Near-infrared to visible upconversion in Er^{3+}-doped $Cs_3Lu_2Cl_9$, $Cs_3Lu_2Br_9$, and $Cs_3Y_2I_9$ excited at 1.54 μm

Stefan R. Lüthi,* Markus Pollnau, and Hans U. Güdel
Departement für Chemie und Biochemie, Universität Bern, Freiestrasse 3, 3000 Bern 9, Switzerland

Markus P. Hehlen†
Optical Sciences Laboratory, University of Michigan, 1301 Beal Avenue, Ann Arbor, Michigan 48109-2122
(Received 10 February 1999)

A detailed study of upconversion processes in $Cs_3Er_2X_9$ ($X=$Cl, Br, I) crystals and in the diluted systems $Cs_3Lu_2Cl_9$:1% Er^{3+}, $Cs_3Lu_2Br_9$:1% Er^{3+}, and $Cs_3Y_2I_9$:1% Er^{3+} is presented. Efficient two-, three-, and four-step upconversion excitation along the sequence $^4I_{15/2}\rightarrow{}^4I_{13/2}\rightarrow{}^4I_{9/2}\rightarrow{}^4S_{3/2}\rightarrow{}^2H_{9/2}$ leading to luminescence throughout the visible and near UV is demonstrated using a 1.54-μm excitation wavelength. This stepwise excitation is possible due to the low phonon energies and, consequently, the significantly longer lifetime of the $^4I_{9/2}$ intermediate state in these systems relative to oxides and fluorides. The absorption and upconversion luminescence intensities increase along the isostructural series $X=$Cl, Br, I as a result of the decreasing energy of the electric-dipole allowed $4f$-$5d$ transitions and, thus, their increasing influence on the parity forbidden $4f$-$4f$ transitions. The excitation mechanisms in the chloride systems are investigated by time-resolved spectroscopy and the respective dynamics is studied by a rate-equation model. In the diluted sample $^4I_{9/2}\rightarrow{}^4S_{3/2}$ excited-state absorption plays a major role and occurs within 3 cm^{-1} of the ground-state absorption, whereas the dynamics in the concentrated system is dominated by energy-transfer upconversion (ETU) in all excitation steps. Of the 35 most likely ETU processes, eight are found to contribute significantly to the excitation mechanisms in the concentrated system. The excitation pathways leading to red luminescence from $^4F_{9/2}$ are also partly resolved. [S0163-1829(99)06725-9]

I. INTRODUCTION

Near-infrared to visible upconversion is a common phenomenon in Er^{3+}-doped solids, and its many aspects have been studied extensively in the past three decades.[1–3] Various processes can lead to emission at wavelengths shorter than the excitation wavelength with energy-transfer upconversion (ETU) and excited-state absorption (ESA) generally being the most efficient ones in the case of the Er^{3+} ion.[1–3] Excitation of the $^4I_{11/2}$ or $^4I_{9/2}$ excited-state multiplets (see Fig. 1) around 980 and 810 nm, respectively, is commonly used since, besides the availability of powerful Ti:sapphire and semiconductor lasers at these wavelengths, both states are part of a series of energetically almost equally spaced multiplets. The sequences $^4I_{15/2}\rightarrow{}^4I_{11/2}\rightarrow{}^4F_{7/2}$ and $^4I_{15/2}\rightarrow{}^4I_{9/2}\rightarrow{}^2H_{9/2}$ have a spacing of $\sim$10 200 and $\sim$12 200 cm^{-1}, respectively, and allow for ETU and ESA processes to take place efficiently under one-color excitation due to the resonances involved.

A sequence with similarly favorable resonance is $^4I_{15/2}\rightarrow{}^4I_{13/2}\rightarrow{}^4I_{9/2}\rightarrow{}^4S_{3/2}\rightarrow{}^2H_{9/2}$ with a multiplet spacing of $\sim$6500 cm^{-1}, i.e., involving excitation of the $^4I_{13/2}$ excited state around 1.54 μm in the first step. Furthermore, the $^4I_{13/2}$ ground-state absorption (GSA) has an oscillator strength that is about 2 and 12 times higher than for $^4I_{11/2}$ and $^4I_{9/2}$ GSA, respectively, permitting more efficient pump-light absorption and potentially offering an alternative to Yb^{3+},Er^{3+} codoped systems pumped at 980 nm. Although 1.54-μm upconversion may efficiently populate excited states emitting in the visible and near UV region, it has received much less attention in the past mainly for practical reasons related to generating laser radiation of adequate power and tunability in the 1.54-μm wavelength range. However, with the implementation of optically amplified tunable diode lasers or nonlinear optical laser systems this restriction is currently becoming less stringent.

Studies on upconversion using 1.54-μm excitation have concentrated on the Er^{3+}-doped fluorides $BaYF_5$,[4] BaY_2F_8,[5,6] YF_3,[5,7] $LiYF_4$,[8–13] CaF_2,[8,14–16] SrF_2,[8,17] CdF_2,[17–19] fluoroindate glass,[20–22] and vitroceramics[5,23,24] as well as the oxides $Y_3Al_5O_{12}$ (YAG),[8] $YAlO_3$,[25] and silica glass.[26] Laser action was achieved in 1.54-μm pumped CaF_2,[8,14,16] SrF_2,[8] $LiYF_4$,[8,10,12,13] BaY_2F_8,[6] and YAG (Ref. 8) on the $^4I_{11/2}\rightarrow{}^4I_{13/2}$ transition around 2.8 μm and, in some cases, on various other transitions originating from $^4S_{3/2}$, $^2H_{9/2}$, and $^2P_{3/2}$ with wavelengths in the 1700–407 nm range. The $^2P_{3/2}\rightarrow{}^4I_{11/2}$ laser transition at 469.7 nm in $LiYF_4$ is particularly remarkable since it involves the accumulation of at least five $^4I_{13/2}$ excitations to populate the $^2P_{3/2}$ initial state at $\sim$31 400 cm^{-1}.[12,27] This is an illustration for complex upconversion dynamics being efficient enough to sustain laser action given the existence of adequate resonances and optimal radiative and nonradiative decay properties of the involved intermediate states.

One such key intermediate state is $^4I_{9/2}$, the state that is reached by the first upconversion step from $^4I_{13/2}$ (see Fig. 1). Rapid multiphonon relaxation from $^4I_{9/2}\rightarrow{}^4I_{11/2}$ is a property common to all fluorides and oxides, and the second upconversion step, therefore, predominantly occurs from $^4I_{11/2}$ by (i) another, nonresonant energy transfer from a

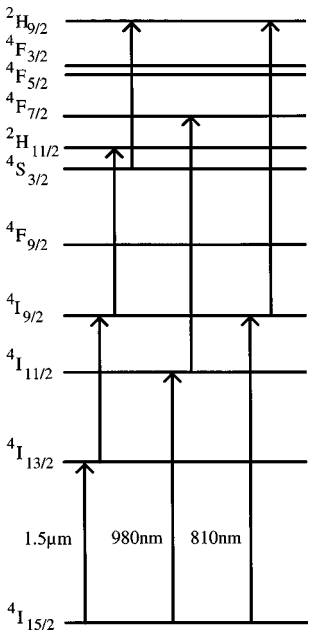

FIG. 1. Schematic energy-level diagram of Er^{3+} up to 25 000 cm^{-1}, indicating possible upconversion steps under pump excitation at 1.5 μm (left-hand side), 980 nm (center), and 810 nm (right-hand side).

nearby ion in the $^4I_{13/2}$ state to reach $^4F_{9/2}$, i.e., $(^4I_{11/2}, ^4I_{13/2}) \rightarrow (^4F_{9/2}, ^4I_{15/2})$, followed by red emission, or by (ii) the interaction of two nearby ions in the $^4I_{11/2}$ state to reach $^4F_{7/2}$, i.e., $(^4I_{11/2}, ^4I_{11/2}) \rightarrow (^4F_{7/2}, ^4I_{15/2})$, followed by multiphonon relaxation and green emission from $^4S_{3/2}$.[2,3] Thus, upconversion processes do not directly proceed along the ~6500 cm^{-1} spaced multiplet sequence $^4I_{15/2} \rightarrow ^4I_{13/2} \rightarrow ^4I_{9/2} \rightarrow ^4S_{3/2} \rightarrow ^2H_{9/2}$ in these compounds but rather branch into various other channels after the first upconversion step. This is different in materials with low-energy optical phonons, such as chlorides, bromides, and iodides, where multiphonon relaxation of $^4I_{9/2}$ is negligible.[2,3] Ohwaki *et al.* have studied powders of the Er^{3+}-doped phosphors $BaCl_2$, YCl_3-$PbCl_2$-KCl, YBr_3, and YI_3 under 1.52-μm excitation at room temperature, and they attributed the strongly enhanced visible luminescence intensity relative to fluoride phosphors in part to low $^4I_{9/2}$ multiphonon relaxation.[28–30] However, no detailed analysis of 1.54-μm upconversion processes in low-energy phonon materials has been reported to date.

In this paper we present a study of upconversion processes in $Cs_3Lu_2Cl_9$:1% Er^{3+}, $Cs_3Lu_2Br_9$:1% Er^{3+}, $Cs_3Y_2I_9$:1% Er^{3+}, and $Cs_3Er_2X_9$ (X=Cl, Br, I) crystals excited around 1.54 μm. This family of compounds allows for variation of both the Er^{3+} ion density and the maximum optical phonon frequency without substantially varying the structure. In addition, frequency- and time-domain spectroscopy in combination with the available extensive energy-level[31–34] and radiative-decay[35] data for these systems provides the basis for detailed experimental and theoretical insight into the dynamics of various upconversion processes and their competition in these materials.

It is found that in addition to decreasing optical phonon frequencies along X=Cl, Br, I also decreasing crystal-field strengths contribute significantly to the suppression of $^4I_{9/2}$ multiphonon relaxation. Experimental results and numerical analysis show that after a first $(^4I_{13/2}, ^4I_{13/2}) \rightarrow (^4I_{9/2}, ^4I_{15/2})$ ETU step, both ETU and ESA processes may subsequently populate the green emitting multiplets $^4S_{3/2}$ and $^2H_{11/2}$ in the second step, a competition that is mainly a function of Er^{3+} ion density. Further ETU from $^4S_{3/2}$ to the violet-emitting $^2H_{9/2}$ multiplet is, although being highly resonant and exhibiting high dipole strengths of the involved transitions, inefficient at the available pump intensity due to the considerably smaller population densities of the $^4I_{9/2}$ and $^4S_{3/2}$ initial levels of these upconversion processes. The intrinsic green upconversion efficiency for 1.54-μm excitation in these materials that directly follow along the $^4I_{15/2} \rightarrow ^4I_{13/2} \rightarrow ^4I_{9/2} \rightarrow ^4S_{3/2} \rightarrow ^2H_{9/2}$ multiplet sequence is at least 25% higher than for fluorides and oxides.

II. EXPERIMENT

A. Sample preparation

$Cs_3R_2X_9$ (R=Er, Lu; X=Cl, Br) represent incongruently melting phases of the binary halides CsX and RX_3.[36,37] Since Er^{3+} (0.881 Å) has an ionic radius comparable to Lu^{3+} (0.848 Å), it can be doped into $Cs_3Lu_2X_9$ by replacing stoichiometric amounts of LuX_3 by ErX_3.[38] Dry RX_3 powders were prepared from R_2O_3 (Rhone Poulenc, 99.999%) using the NH_4X method.[39] RX_3 and CsX (Merck, suprapur) were sublimed in boron-nitride ampoules for additional purification. Starting from CsX, LuX_3, and ErX_3, single crystals of $Cs_3Er_2X_9$ and $Cs_3Lu_2X_9$:1% Er^{3+} were grown in silica ampoules by the Bridgman technique.

$Cs_3M_2I_9$ (M=Er, Y) represent congruently melting phases of CsI and MI_3.[40] As in the case of Lu^{3+}, Er^{3+} substitutes for Y^{3+} (0.88 Å) in $Cs_3Y_2I_9$:1% Er^{3+} without changing the crystal structure of the compound. The preparation of $Cs_3Er_2I_9$ and $Cs_3Y_2I_9$:1% Er^{3+} started with the synthesis of pure $Cs_3Y_2I_9$ and $Cs_3Er_2I_9$. Since the NH_4X method cannot be used to prepare ErI_3,[39,41] the synthesis of $Cs_3M_2I_9$ was performed using CsI, I_2, and the elemental M as starting materials. Stoichiometric amounts of CsI (Merck, 99% pure), I_2 (Merck, 99.5% pure), and M powders (Cerac, 99.99% pure) were filled into silica ampoules and sealed off under vacuum. The ampoules were put in horizontal position in a furnace and heated to 200 °C for two days to allow for complete reaction to $Cs_3M_2I_9$. The obtained $Cs_3M_2I_9$ powders were sublimed in silica ampoules in a final purification step. Single crystals of pure $Cs_3Er_2I_9$ and of $Cs_3Y_2I_9$:1% Er^{3+} were grown from pure $Cs_3Er_2I_9$ and from a stoichiometric mixture of $Cs_3Y_2I_9$ and $Cs_3Er_2I_9$, respectively, sealed in silica ampoules under vacuum by the Bridgman technique.

The high hygroscopicity of the starting materials as well as the final compounds themselves required synthesis, crystal growth, and sample preparation to be carried out in a dry inert atmosphere.

B. Spectroscopic measurements

All luminescence and lifetime measurements were carried out on crystallographically unoriented $Cs_3Lu_2X_9$:Er^{3+} (X=Cl, Br) and $Cs_3Y_2I_9$:Er^{3+} single crystals that were sealed in silica ampoules under dry helium gas to provide for sufficient thermal contact and a moisture-free atmosphere. The

ampoules were contact-mounted in a cold-finger cryostat cooled by liquid nitrogen for the low-temperature measurements.

Continuous-wave (cw), frequency-tunable excitation for the $^4I_{15/2}\rightarrow{}^4I_{13/2}$ transitions of Er^{3+} in the near infrared was provided by a low-power (<1.5 mW) external-cavity tunable diode laser amplified by an optically isolated erbium-doped fiber amplifier (EDFA). The EDFA consisted of a 50-m long, 100-ppm Er^{3+}-doped silica fiber into which the astigmatically corrected diode-laser beam and the pump light from a power-stabilized Ti:sapphire laser (400 mW at 975 nm) were coupled by means of a wavelength division multiplexing coupler, providing for an overall system gain of ~15 dB at 1.54 μm. The Gaussian output beam was passed through a 1.1-μm long-pass interference filter and focused into the sample where the pump intensity was ~100 W cm^{-2} for the cw experiments. For the time-resolved upconversion-luminescence measurements, the 1.54-μm beam from the EDFA was controlled by an acoustooptic modulator driven by a rf frequency synthesizer and a square-wave generator. A pulse width of 100 μs was used at a repetition rate of 15 Hz, corresponding to a duty cycle of 0.15%, and the instrumental time resolution was 2 μs. For $Cs_3Lu_2X_9:Er^{3+}$ (X=Cl, Br) and $Cs_3Y_2I_9:Er^{3+}$ the excitation wavelengths were at 1536.47, 1539.67, and 1539.77 nm, respectively, i.e., excitation of the $^4I_{15/2}(0)\rightarrow{}^4I_{13/2}(0)$ crystal-field transition in each compound.

Sample luminescence was dispersed by a 1-m single monochromator (1200 lines/mm grating) and detected by a cooled photomultiplier in combination with a photon-counting system and a multichannel scaler for the cw and the time-resolved experiments, respectively. The luminescence spectra were corrected for the wavelength-dependent sensitivity of the detection system that was determined by measuring a calibrated tungsten lamp.

Excited-state lifetimes were measured by direct short-pulse excitation of the respective multiplet. For $^4I_{13/2}$, the laser described above was used, and the luminescence was detected by a fast In-Ga-As detector in combination with a digitizing oscilloscope. $^4I_{9/2}$ and $^4S_{3/2}$ were excited by a Nd:YAG-laser-pumped (20 Hz) and Raman Stokes-shifted (H_2, 340 psi) Rhodamin 101 dye laser and a Raman anti-Stokes–shifted (H_2) Pyridin 1 dye laser, respectively, and their luminescence was detected by a cooled photomultiplier in combination with a multichannel scaler.

Absorption cross sections for the Judd-Ofelt calculations were obtained from room-temperature absorption measurements. For this purpose, single crystals of the pure $Cs_3Er_2X_9$ (X=Cl, Br, I) and of 1% Er^{3+}-doped $Cs_3Lu_2Cl_9$, $Cs_3Lu_2Br_9$, and $Cs_3Y_2I_9$, respectively, were sealed in epoxy resin. Plates with parallel surfaces were cut with a diamond saw and polished to optical quality using Al_2O_3 powders of decreasing size down to 0.3 μm suspended in dry paraffin oil. The samples were subsequently mounted in copper cells with silica windows for the spectroscopic measurements.

III. SPECTROSCOPIC RESULTS

Figure 2 presents unpolarized room-temperature survey absorption spectra in the range of 6000–30 000 cm^{-1} for $Cs_3Lu_2Cl_9$ (top), $Cs_3Lu_2Br_9$ (middle), and $Cs_3Y_2I_9$ (bottom) doped with 1% Er^{3+} [Fig. 2(a)] and for the pure compounds $Cs_3Er_2Cl_9$ (top), $Cs_3Er_2Br_9$ (middle), and $Cs_3Er_2I_9$ (bottom) [Fig. 2(b)]. All observed excited-state multiplets are labeled with the respective $^{2S+1}L_J$ ($4f^{11}$) term symbol. In pure $Cs_3Er_2X_9$ (X=Cl, Br, I) the transitions $^4I_{15/2}\rightarrow{}^2H_{11/2}$ and $^4I_{15/2}\rightarrow{}^4G_{11/2}$ exceeded the instrumental absorbance limit even for samples as thin as 0.3 mm. Thus, neither relative nor absolute absorption intensities of these can be compared to other transitions. For all other transitions, respective oscillator strengths of the 1% Er^{3+}-doped and the pure compound are identical to within 10–20 %. The $4f$-$4f$ transition intensities clearly increase along Cl-Br-I due to the decreasing energy of the lowest-energy $4f$-$5d$ transition along the halide series. It is situated around 44 000, 40 000, and 30 000

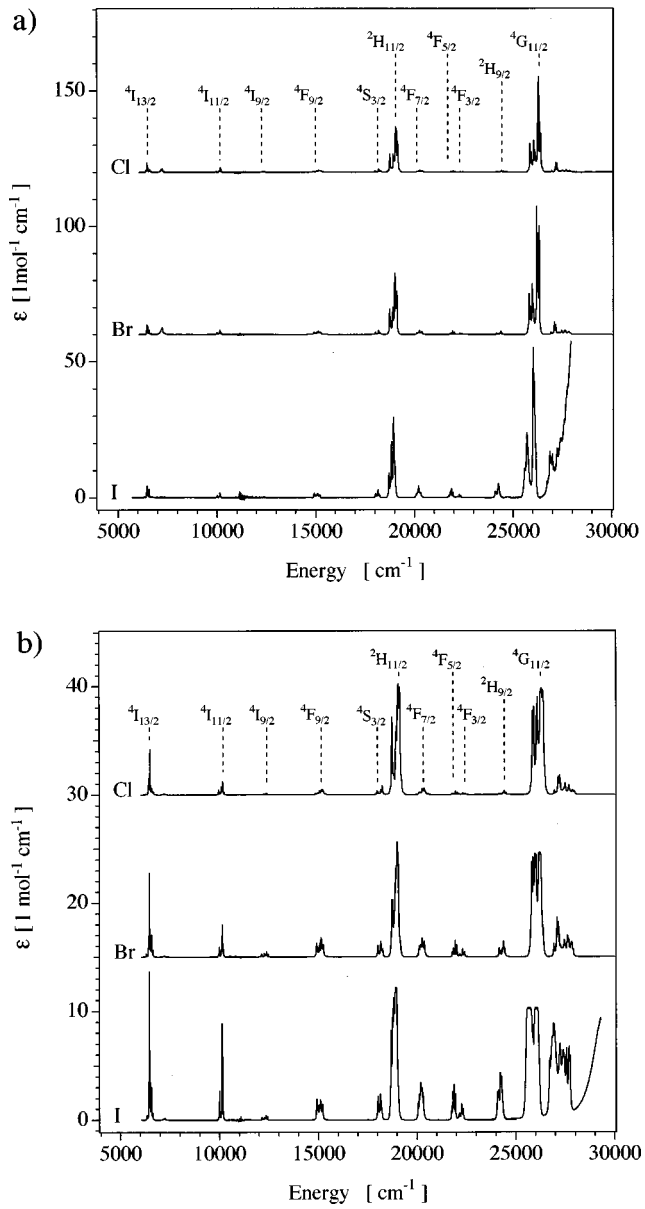

FIG. 2. Unpolarized survey absorption spectra of (a) $Cs_3Lu_2Cl_9$ (top), $Cs_3Lu_2Br_9$ (middle), and $Cs_3Y_2I_9$ (bottom) doped with 1% Er^{3+} and (b) of the pure compounds $Cs_3Er_2Cl_9$ (top), $Cs_3Er_2Br_9$ (middle), and $Cs_3Er_2I_9$ (bottom). All spectra were recorded at 295 K. Multiplet term symbols for all excited states observed in the range of 6000–30 000 cm^{-1} are indicated in the spectra.

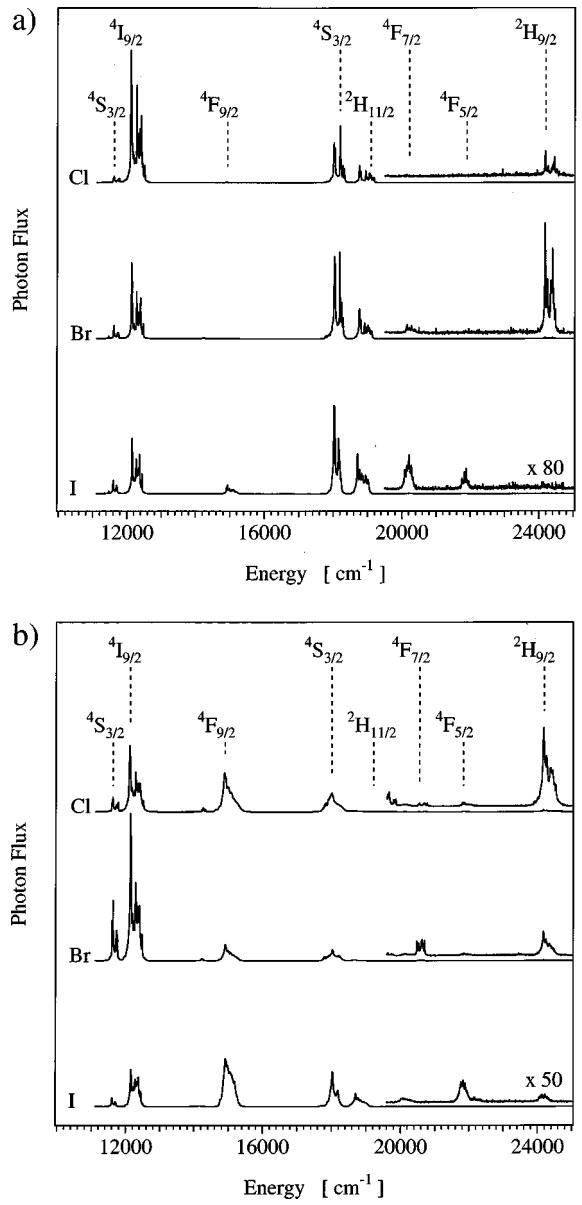

FIG. 3. Unpolarized upconversion-luminescence spectra of (a) $Cs_3Lu_2Cl_9$ (top), $Cs_3Lu_2Br_9$ (middle), and $Cs_3Y_2I_9$ (bottom) doped with 1 % Er^{3+} and (b) of the pure compounds $Cs_3Er_2Cl_9$ (top), $Cs_3Er_2Br_9$ (middle), and $Cs_3Er_2I_9$ (bottom) at 295 K. The samples are excited by the respective $^4I_{15/2}(0)\rightarrow{}^4I_{13/2}(0)$ transition around 1.54 μm. The labeled transitions terminate on the $^4I_{15/2}$ ground-state multiplet except for the $^4S_{3/2}\rightarrow{}^4I_{13/2}$ transition around 11 700 cm^{-1}. The spectra are calibrated and the emission intensity is given in units of photon flux. Since the pumped volume is the same for all luminescences of each spectrum, the ordinate can also be interpreted in terms of relative luminescence rates.

cm^{-1} for the chloride, bromide, and iodide host lattice, respectively. In Fig. 2 we observe the onset of the $4f$-$5d$ absorption above 27 000 cm^{-1} for the iodide compounds. The influence of the $4f$-$5d$ transitions on the $4f$-$4f$ transition intensities is not uniform over the entire spectral range. Rather, it is more pronounced for $4f$ multiplets above 18 000 cm^{-1}, which are more strongly enhanced in the iodide.

Upconversion-luminescence spectra were measured at 77 and 295 K, and the main features were found to be largely temperature independent. Figures 3(a) and 3(b) show spectra for $Cs_3Lu_2X_9$:1% Er^{3+} (X=Cl, Br), $Cs_3Y_2I_9$:1% Er^{3+} and $Cs_3Er_2X_9$ (X=Cl, Br, I), respectively, at 295 K in units of photon flux. Excitation is around 1.54 μm with the laser tuned in resonance with the respective crystal-field transition from the lowest level of the $^4I_{15/2}$ ground-state multiplet to the lowest level of the $^4I_{13/2}$ first excited-state multiplet, i.e., $^4I_{15/2}(0)\rightarrow{}^4I_{13/2}(0)$. Intense visible upconversion luminescence is observed from all the samples. In $Cs_3Lu_2X_9$:1% Er^{3+} (X=Cl, Br) and $Cs_3Y_2I_9$:1% Er^{3+} [see Fig. 3(a)] emission from $^4I_{9/2}$ and $^4S_{3/2}/{}^2H_{11/2}$ is dominant and is the result of a one- and two-step upconversion process (see Fig. 1), respectively. Since the human eye is insensitive at the $^4I_{9/2}$ emission wavelengths, the luminescence from these samples is a highly saturated bright green centered at 555 nm. The undiluted $Cs_3Er_2X_9$ (X=Cl, Br, I) samples [Fig. 3(b)] show additional contributions from $^4F_{9/2}$ in the red spectral region which is being populated by cross-relaxation processes that are suppressed in the diluted samples. Luminescence in the blue spectral range is weak for all the samples. In particular, the low emission rate from $^2H_{9/2}$, which can be populated by a four-step upconversion process (see Fig. 1), is striking. The $^2H_{11/2}$ versus $^4S_{3/2}$ luminescence-rate ratio decreases with decreasing temperature from 0.451 and 0.408 at 295 K to 0.0542 and 0.0474 at 77 K (spectrum not shown) for X =Cl, Br, respectively, indicating a thermal equilibrium of these two states. This is not the case for the iodide system where the trend is even opposite with a ratio of 0.680 and 0.866 at 295 and 77 K, respectively, thus indicating a decreasing multiphonon-relaxation rate with decreasing temperature.

Figures 4(a) and 4(b) show measured power dependences (left-hand side) of various upconversion-luminescence transitions to the $^4I_{15/2}$ ground-state multiplet in $Cs_3Lu_2Cl_9$:1% Er^{3+} and $Cs_3Er_2Cl_9$ at 77 K, respectively. The initial slopes in $Cs_3Lu_2Cl_9$:1% Er^{3+} are close to 2 for the excitation of $^4I_{9/2}$, 3 for $^4S_{3/2}$ and $^4F_{9/2}$, and 4 for $^2H_{9/2}$. However, in $Cs_3Lu_2Cl_9$:1% Er^{3+} at higher pump powers and clearly in $Cs_3Er_2Cl_9$ the slopes deviate significantly from these values. In $Cs_3Er_2Cl_9$ the slope for the $^2H_{9/2}$ luminescence converges to one at higher pump power, whereas the slopes of the other luminescences are even smaller than one.

Table I presents decay-time constants of the $^4I_{13/2}$, $^4I_{9/2}$, and $^4S_{3/2}$ excited-state multiplets in $Cs_3Lu_2Cl_9$:1% Er^{3+} and $Cs_3Er_2Cl_9$ at 77 and 295 K as observed after direct, short-pulse excitation of the respective states. These states are the intermediate excited states for 1.54-μm-pumped upconversion along the sequence $^4I_{15/2}\rightarrow{}^4I_{13/2}\rightarrow{}^4I_{9/2}\rightarrow{}^4S_{3/2}\rightarrow{}^2H_{9/2}$. Whereas the $^4I_{13/2}$ lifetime is essentially the same for $Cs_3Lu_2Cl_9$:1% Er^{3+} and $Cs_3Er_2Cl_9$ at both temperatures, the $^4I_{9/2}$ and $^4S_{3/2}$ lifetimes are strongly concentration quenched in $Cs_3Er_2Cl_9$ at room temperature. Data of the radiative lifetimes obtained from the Judd-Ofelt calculation are also given.[33]

Upconversion transients for the two transitions $^4I_{9/2}\rightarrow{}^4I_{15/2}$ (826 nm) and $^4S_{3/2}\rightarrow{}^4I_{15/2}$ (555 nm) were measured at 77 and 295 K, again showing no significant temperature dependence. Figures 5(a) and 5(b) show transient measurements (left-hand side) for $Cs_3Lu_2Cl_9$:1% Er^{3+} and $Cs_3Er_2Cl_9$ at 295 K, respectively. The laser-pulse energy incident on the sample was as low as 750 nJ, explaining increased noise in

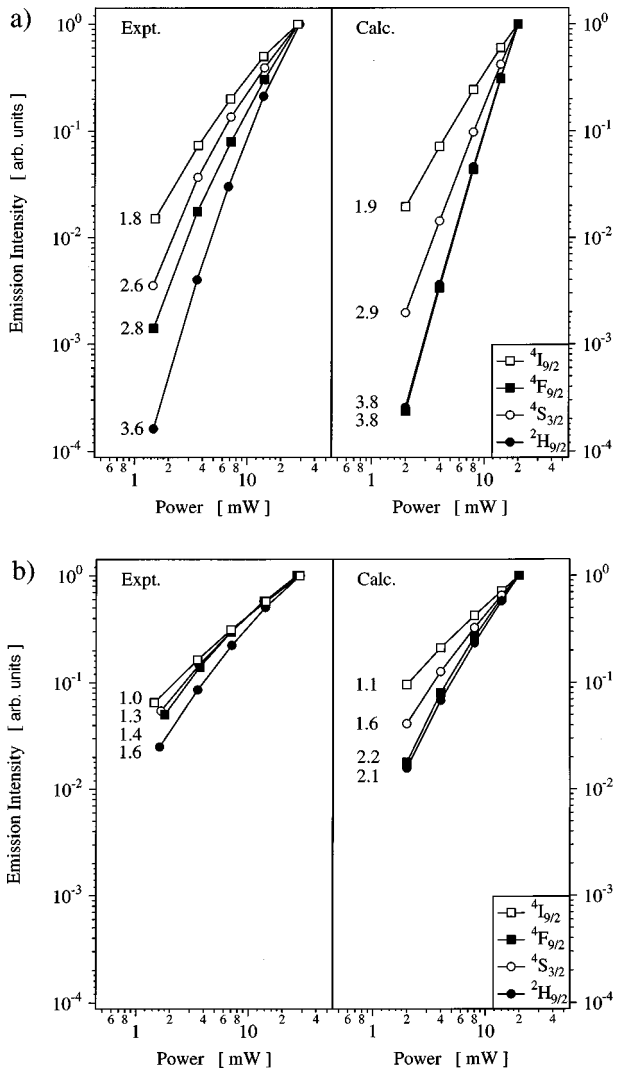

FIG. 4. Power dependence of various luminescence transitions to the $^4I_{15/2}$ ground-state multiplet in (a) $Cs_3Lu_2Cl_9$:1% Er^{3+} and (b) $Cs_3Er_2Cl_9$ excited by the $^4I_{15/2}(0)\rightarrow{}^4I_{13/2}(0)$ transition at 1.536 μm: experimental data at 77 K (left-hand side) and numerical data calculated from the rate-equation model (right-hand side). The initial slopes, determined from the double logarithmic representation of the data, are indicated.

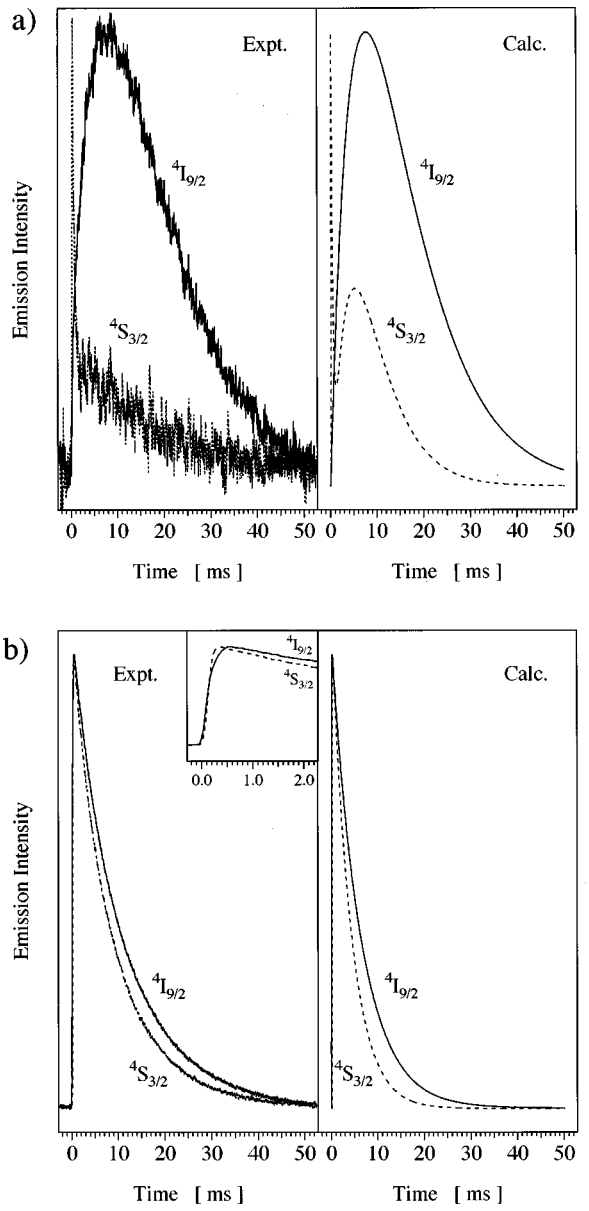

FIG. 5. Upconversion luminescence transients of the $^4I_{9/2}\rightarrow{}^4I_{15/2}$ (826 nm) and $^4S_{3/2}\rightarrow{}^4I_{15/2}$ (555 nm) transitions of (a) $Cs_3Lu_2Cl_9$:1% Er^{3+} and (b) $Cs_3Er_2Cl_9$ excited at $t=0$ ms by a 100-μs square pulse on the $^4I_{15/2}(0)\rightarrow{}^4I_{13/2}(0)$ transition at 1.536 μm: Experimental data at 295 K (left-hand side). The inset shows the rise characteristics of the respective transients. Numerical data calculated from the rate-equation model (right-hand side).

TABLE I. Decay times of selected excited-state multiplets in $Cs_3Lu_2Cl_9$:1% Er^{3+} and $Cs_3Er_2Cl_9$ at 77 and 295 K observed after direct, short-pulse excitation of the respective states. The values were obtained from least-squares fits of a single exponential and are given in units of (ms). The last column gives radiative lifetimes calculated from the Judd-Ofelt model using the parameters $\Omega_2=8.61$, $\Omega_4=0.423$, $\Omega_6=0.227$ (10^{-20} cm^{-2}) and a refractive index of $n=1.82$ (Ref. 33).

	$Cs_3Lu_2Cl_9$:1% Er^{3+}		$Cs_3Er_2Cl_9$		
Multiplet	295 K	77 K	295 K	77 K	Judd-Ofelt model
$^4I_{13/2}$	12.3	13.1	14.4	15.7	9.2
$^4I_{9/2}$	9.8	9.4	0.046	10.2	16.0
$^4S_{3/2}$	0.39	0.5	0.0054	0.8	2.1

the transients of the weakly absorbing 1% sample [Fig. 5(a)]. For both samples, the $^4I_{9/2}$ transient exhibits a rise and slow decay after the excitation pulse indicative of an ETU process populating the $^4I_{9/2}$ multiplet. This is also the case for the $^4S_{3/2}$ transient in $Cs_3Er_2Cl_9$. The transients of both the $^4I_{9/2}$ and $^4S_{3/2}$ luminescences are very similar in $Cs_3Er_2Cl_9$, with a very fast rise and a relatively slow decay. The rise of $^4I_{9/2}$ luminescence in the diluted sample is more than one order of magnitude slower. In contrast, the $^4S_{3/2}$ transient in $Cs_3Lu_2Cl_9$:1% Er^{3+} exhibits a very different behavior at both temperatures. An instantaneous rise within the experimental time resolution and a subsequent fast decay is indicative of an ESA process populating this level. This is followed

TABLE II. Average $^4I_{9/2} \rightarrow {}^4I_{11/2}$ energy gap for oxides and halides compiled from various literature sources. $\hbar\omega_{max}$ is the highest optical phonon energy. Values for both, average energy gap and phonon energies are given in (cm^{-1}). p_{min} is the minimum number of phonons required to bridge the $^4I_{9/2} \rightarrow {}^4I_{11/2}$ gap. k_{mp} is the estimated multiphonon-relaxation rate constant, k_{rad} is the estimated radiative rate constant, and k_{tot} is the sum of both. η_q is the radiative quantum yield of the $^4I_{9/2}$ level.

	Oxide	Fluoride	Chloride	Bromide	Iodide
Avg. gap	1894	2036	2117	2135	2138
$\hbar\omega_{max}$	600	355	260	172	144
p_{min}	3.1	5.8	8.1	12.3	14.9
k_{mp} (s^{-1})	1.25×10^{6}	3.18×10^{4}	8×10^{-3}	2×10^{-8}	$<1\times10^{-8}$
k_{rad} (s^{-1})			200–1000		
$\eta_q = k_{rad}/k_{tot}$	$<8\times10^{-4}$	$<3\times10^{-2}$	~1	~1	~1

by a slow decay with a decay time similar to that of the $^4I_{9/2}$ transient.

IV. INFLUENCE OF OPTICAL PHONON ENERGY

In this section, we investigate the influence of the optical phonon energy along the series O, F, Cl, Br, I on the $^4I_{9/2}$ lifetime and on the thermal coupling of the $^2H_{11/2}/{}^4S_{3/2}$ states.

A. $^4I_{9/2}$ energy gap trend

The upconversion efficiency using excitation of the erbium ion at 1.54 μm along the multiplet sequence $^4I_{15/2} \rightarrow {}^4I_{13/2} \rightarrow {}^4I_{9/2} \rightarrow {}^4S_{3/2} \rightarrow {}^2H_{9/2}$ depends critically on the storage capacity of the intermediate excited states, i.e., on the lifetimes of these levels. Radiative rate constants of f-f transitions in erbium are similar for different host materials. The rate constants for multiphonon relaxation, on the other hand, vary by orders of magnitude with the optical phonon energy of the host material. This is a result of the exponential dependence of the multiphonon-relaxation rate constant on the number of phonons emitted in the relaxation to the next lower-lying level.

The intermediate excited state that is most affected by multiphonon decay in the above sequence is $^4I_{9/2}$ because of its smallest energy gap to the next lower-lying level $^4I_{11/2}$. The energy gap relevant for multiphonon decay is the energy difference between the lowest crystal-field level of $^4I_{9/2}$ and the highest crystal-field level of $^4I_{11/2}$. From various literature sources this energy gap for different Er^{3+}-doped host materials is found to be YAG=1880 cm^{-1};[42] YSGG=1917 cm^{-1};[42] YSAG=1885 cm^{-1};[42] LaF_3 =2024 cm^{-1};[43] YLF=2049 cm^{-1};[44,45] Cs_2NaYCl_6 =2089 cm^{-1};[46] $Cs_3Lu_2Cl_9$=2115 cm^{-1};[31] $LaCl_3$ =2148 cm^{-1};[47] $CsCdBr_3$=2138 cm^{-1};[48] $Cs_3Lu_2Br_9$ =2133 cm^{-1};[32] $Cs_3Y_2I_9$=2138 cm^{-1}.[33] This yields average $^4I_{9/2}$-$^4I_{11/2}$ energy gaps for the different classes of host materials of: oxide=1894 cm^{-1}; fluoride=2036 cm^{-1}; chloride =2117 cm^{-1}; bromide=2135 cm^{-1}; iodide=2138 cm^{-1}, i.e., an increase of 13% from oxide to iodide. Since the decreasing orbital angular momentum with increasing covalency from oxide to iodide reduces rather than increases the $^4I_{9/2}$-$^4I_{11/2}$ barycenter energy splitting, the observed trend is the result of decreasing crystal-field splittings of both multiplets due to a decreasing crystal-field strength along O, F, Cl, Br, I.

As shown in Table II, the highest optical phonon energy drops by 75% along the series O, F, Cl, Br, I. Both trends, increasing energy gap and decreasing optical phonon energy, add up in terms of minimum number of phonons p that is necessary to bridge the $^4I_{9/2}$-$^4I_{11/2}$ energy gap. An estimate of the radiative quantum yield η_q of the $^4I_{9/2}$ level is obtained from calculating the multiphonon-relaxation rate constant k_{mp} for the various materials using the parameters given in Ref. 49 and comparing it to the estimated radiative relaxation rate constant k_{rad}. The η_q values in Table II indicate that between fluoride and chloride the relative importance of multiphonon and radiative decay reverses. In the heavier halides, the $^4I_{9/2}$ lifetime is significantly increased, leading to fundamentally different 1.5-μm upconversion dynamics in chloride/bromide/iodide as compared to oxide/fluoride systems.

B. Thermal coupling of $^2H_{11/2}$ and $^4S_{3/2}$

Excitation reaching $^2H_{11/2}$ is expected to relax predominantly by multiphonon relaxation due to the small energy gap to $^4S_{3/2}$ which equals 2.7, 4.1, and 4.6 highest-energy phonons in Cl, Br, and I, respectively (see Fig. 1). However, the $^2H_{11/2} \rightarrow {}^4I_{15/2}$ transition has a high oscillator strength compared to $^4S_{3/2} \rightarrow {}^4I_{15/2}$ (see Fig. 2), and radiative relaxation might, therefore, be competitive. The quantity

$$r(T) \equiv \frac{I_{^2H_{11/2}}(T)}{I_{^4S_{3/2}}(T)} \propto \frac{\sum_{i=3}^{8} n_i(T) f_i}{\sum_{i=1}^{2} n_i(T) f_i} \qquad (1)$$

is a measure for the $^2H_{11/2}$ vs $^4S_{3/2}$ luminescence intensity ratio as a function of temperature. For the combined eight Kramers degenerate crystal-field levels of $^4S_{3/2}$ and $^2H_{11/2}$ in thermal equilibrium, the relative level populations are given by the Boltzmann factors n_i (T), and luminescence rates are subsequently obtained by multiplication of n_i (T) by the respective oscillator strengths f_i for the transitions to the eight Kramers degenerate crystal-field levels of the $^4I_{15/2}$ ground-state multiplet. f_i values have been estimated in Ref. 50 for an oxide system and we assume these values to be representative for our three systems. For Cl, Br, and I luminescence-rate ratios of 7.0×10^{-6}, 9.6×10^{-6}, and 1.8×10^{-5}, are calculated from Eq. (1) for thermal equilibrium

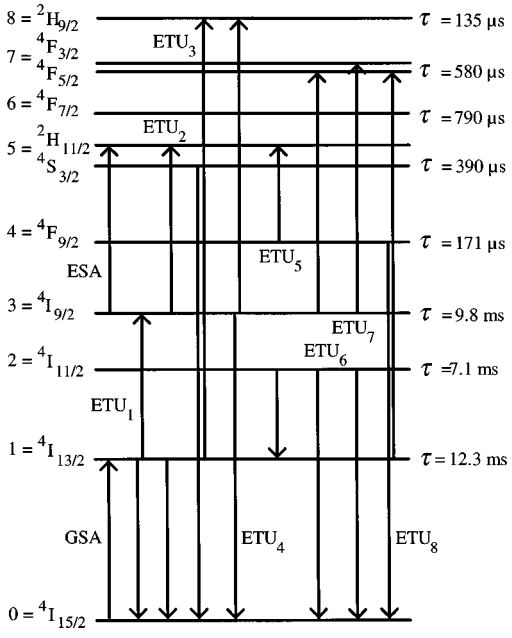

FIG. 6. Schematic energy-level diagram of Er^{3+} up to 25 000 cm^{-1}, indicating GSA into $^4I_{13/2}$ and ESA from $^4I_{9/2}$ at 1.54 μm as well as important ETU processes for $Cs_3Lu_2Cl_9$:1% Er^{3+} and $Cs_3Er_2Cl_9$. The ETU processes are shown in the direction of upconversion. If two pathways are possible, the pathway with the higher oscillator strengths is shown. The lifetimes of the $^4I_{13/2}$, $^4I_{9/2}$, and $^4S_{3/2}$ levels are values measured for $Cs_3Lu_2Cl_9$:1% Er^{3+}. The other values are the inverse radiative emission rates obtained from a Judd-Ofelt calculation for the same host.

at 77 K, respectively. These values are significantly smaller than the experimentally observed luminescence-rate ratios by factors of 7.7×10^3, 4.9×10^3, and 4.8×10^4, for these three systems, respectively, providing clear indication for the two multiplets not being in thermal equilibrium at 77 K. This is particularly pronounced for the iodide which requires the most phonons for bridging the $^2H_{11/2}$-$^4S_{3/2}$ energy gap. At room temperature, equilibrium luminescence-rate ratios of 0.29, 0.32, and 0.37 are expected from Eq. (1), and they are only ~30–80 % higher than the experimentally observed ratios of 0.45, 0.41, and 0.68 for Cl, Br, and I [from Fig. 3(a)], respectively. Given the crude assumption for the f_i values in evaluating Eq. (1), this apparent deviation from thermal equilibrium is not substantial. Therefore, assuming a thermal equilibrium for the $^4S_{3/2}$ and $^2H_{11/2}$ multiplets and treating them as one level in our model calculations at room temperature for the chloride system (see Fig. 6, Sec. V, and Appendixes A and B) is justified. In this case, ESA and ETU processes that populate $^2H_{11/2}$ will, therefore, simultaneously populate $^4S_{3/2}$, and luminescence from both multiplets will exhibit identical transient behavior.

V. RATE-EQUATION SOLUTIONS

It is our goal to understand the relative rates (Fig. 3), the power dependence (Fig. 4), and the transient behavior (Fig. 5) of upconversion luminescence in the chloride system and to identify the excitation and relaxation processes which are most important under 1.54-μm pumping. In order to reach this goal, we solved the rate equations describing the excitation and relaxation mechanisms in $Cs_3Lu_2Cl_9$:1% Er^{3+} and $Cs_3Er_2Cl_9$. The spatially resolved rates of the investigated processes and population densities of the states indicated in Fig. 6 were derived for cw and pulsed excitation and for the two dopant concentrations.

A. Computer model

As explained in detail in the Appendixes, we considered the ground state and eight excited states (Fig. 6), pump power and pump configuration, GSA and ground-state bleaching, ESA, all lifetimes and branching ratios, 35 ETU processes, and the crystal data in the rate-equation calculation. Throughout this paper, when using the abbreviation ''ETU,'' we imply both directions of an ETU process, namely upconversion and its inverse process, cross relaxation. The $^4S_{3/2}$ and $^2H_{11/2}$ multiplets as well as the $^4F_{5/2}$ and $^4F_{3/2}$ multiplets were treated as combined levels in thermal equilibrium. Parameters were evaluated and calculations were performed for room temperature. The modeling of the ETU processes is described in Appendix A and the system parameters and rate equations are presented in Appendix B.

For the 100% sample, all relevant parameters could be fixed and the calculation was performed without any fit parameter. For the 1% sample, on the other hand, there remained an uncertainty in two important parameters. First, the ETU transfer parameters W_t of Eq. (A6) of Appendix A had to be adjusted for the 1% Er^{3+} concentration by using the measured concentration dependence of a single ETU parameter in $LiYF_4$:Er^{3+} (cf. Appendix A). Second, the ESA cross section which is relevant for the dynamics in the 1% sample (see later in Sec. VI) remained unknown and was used as a free fit parameter to reproduce the measured transient of the $^4S_{3/2}$ luminescence in $Cs_3Lu_2Cl_9$:1% Er^{3+} [Fig. 5(a)].

B. Comparison of experimental and calculated results

The measured relative rates of the upconversion luminescences from $^4I_{9/2}$, $^4F_{9/2}$, $^4S_{3/2}$, and $^2H_{9/2}$ to the ground state (Fig. 3) and the corresponding calculated luminescence rates as derived from the solution of the rate equations of Appendix B (Table III) are compared in Table IV. The agreement is reasonable, but not overwhelming. For both the 100% and the 1% samples the weak transitions are clearly identified by the calculation. This is also true for the strongest $^4I_{9/2}\rightarrow{}^4I_{15/2}$ transition in the 1% sample. In the 100% system, however, the luminescence rate of this important transition is underestimated by an order of magnitude relative to the luminescence rate of the $^4S_{3/2}\rightarrow{}^4I_{15/2}$ transition. We ascribe this to the uncertainties in the ETU parameters W_{UC} and W_{CR} (Table VI of Appendix A), which can be approximated to within an order of magnitude.

Figure 4 compares the measured and calculated power dependence of upconversion-luminescence transitions from the $^4I_{9/2}$, $^4F_{9/2}$, $^4S_{3/2}$, and $^2H_{9/2}$ to the $^4I_{15/2}$ ground-state multiplet in $Cs_3Lu_2Cl_9$:1% Er^{3+} [Fig. 4(a)] and $Cs_3Er_2Cl_9$ [Fig. 4(b)]. For both $Cs_3Lu_2Cl_9$:1% Er^{3+} and $Cs_3Er_2Cl_9$ the agreement is excellent. Only the power dependence of the $^4F_{9/2}$ luminescence is overestimated in the calculation.

Figure 5 compares measured and calculated upconversion transients of the two transitions $^4I_{9/2}\rightarrow{}^4I_{15/2}$ (826 nm) and

TABLE III. Calculated rates R of the important processes at 1% and 100% dopant concentration for the highest available pump power of 20 mW within the first 2% of the crystal length (first longitudinal element of the spatial resolution; cf. Appendix B). All parameters used in the calculation are given in Appendix B. ETU parameters are given in Table VI of Appendix A. The ETU rates are calculated from Eq. (A7). A negative ETU rate indicates an ETU process being stronger in the cross-relaxation direction. The values in brackets are the rates in the upconversion direction. LUM=ground-state luminescence.

Process	Relaxation	Excitation	R (1%) ($10^{22}/m^3$ s)		R (100%) ($10^{26}/m^3$ s)	
GSA		$^4I_{15/2}\rightarrow{}^4I_{13/2}$		29310		307.6
ESA		$^4I_{9/2}\rightarrow{}^2H_{11/2}$		23.7		3.9
ETU_1	$^4I_{13/2}\rightarrow{}^4I_{15/2}$	$^4I_{13/2}\rightarrow{}^4I_{9/2}$	(65.0)	64.9	(1604)	2.0
ETU_2	$^4I_{13/2}\rightarrow{}^4I_{15/2}$	$^4I_{9/2}\rightarrow{}^2H_{11/2}$	(1.2)	1.2	(3650)	185.0
ETU_3	$^4S_{3/2}\rightarrow{}^4I_{15/2}$	$^4I_{13/2}\rightarrow{}^2H_{9/2}$	(6.0×10^{-3})	6.0×10^{-3}	(189.3)	118.1
ETU_4	$^4I_{9/2}\rightarrow{}^4I_{15/2}$	$^4I_{9/2}\rightarrow{}^2H_{9/2}$	(1.4×10^{-3})	1.3×10^{-3}	(472.2)	-114.8
ETU_5	$^4I_{11/2}\rightarrow{}^4I_{13/2}$	$^4F_{9/2}\rightarrow{}^2H_{11/2}$	(2.8×10^{-11})	-1.3×10^{-3}	(24.8)	-14.8
ETU_6	$^4I_{11/2}\rightarrow{}^4I_{15/2}$	$^4I_{9/2}\rightarrow{}^4F_{5/2}$	(2.5×10^{-6})	2.5×10^{-6}	(14.5)	13.8
ETU_7	$^4I_{11/2}\rightarrow{}^4I_{15/2}$	$^4I_{9/2}\rightarrow{}^4F_{3/2}$	(2.5×10^{-6})	2.5×10^{-6}	(14.8)	13.2
ETU_8	$^4F_{9/2}\rightarrow{}^4I_{15/2}$	$^4I_{13/2}\rightarrow{}^4F_{5/2}$	(1.6×10^{-8})	-1.5×10^{-8}	(7.1)	-32.0
LUM_1	$^4I_{13/2}\rightarrow{}^4I_{15/2}$			29200		45.9
LUM_2	$^4I_{11/2}\rightarrow{}^4I_{15/2}$			1.4		4.4
LUM_3	$^4I_{9/2}\rightarrow{}^4I_{15/2}$			31.8		5.9
LUM_4	$^4F_{9/2}\rightarrow{}^4I_{15/2}$			1.4×10^{-3}		38.5
LUM_5	$^2H_{11/2}/{}^4S_{3/2}\rightarrow{}^4I_{15/2}$			16.7		33.5
LUM_6	$^4F_{7/2}\rightarrow{}^4I_{15/2}$			1.6×10^{-5}		3.2×10^{-2}
LUM_7	$^4F_{3/2}/{}^4F_{5/2}\rightarrow{}^4I_{15/2}$			2.0×10^{-6}		2.3×10^{-2}
LUM_8	$^2H_{9/2}\rightarrow{}^4I_{15/2}$			3.8×10^{-4}		9.4×10^{-2}

$^4S_{3/2}\rightarrow{}^4I_{15/2}$ (555 nm) for $Cs_3Lu_2Cl_9$:1% Er^{3+} [Fig. 5(a)] and $Cs_3Er_2Cl_9$ [Fig. 5(b)]. The pronounced difference in the measured transients for $Cs_3Lu_2Cl_9$:1% Er^{3+} and $Cs_3Er_2Cl_9$ is well reproduced in the calculation. The results for the 100% sample show a slightly faster decay of both luminescence intensities in the calculation compared to the measurement. The behavior of the transients relative to each other, however, is very well reproduced. The $^4S_{3/2}$ transient of the 1% sample has a very peculiar shape, with a very sharp spike and a long tail extending out to 40 ms. It is remarkable that the model reproduces the essential features of this behavior. Quantitatively, the agreement is not perfect; the long-lived component has a larger relative intensity and shorter lifetime in the calculation compared to the measurement. This deviation is explained partly by the uncertainty in the ESA cross section and the transfer parameters W_t for the 1% sample which determine the relative height of the two peaks in the $^4S_{3/2}$ transient (see later in Sec. VI).

TABLE IV. Comparison of the experimental ground-state luminescence rates for $Cs_3Lu_2Cl_9$:1% Er^{3+} and $Cs_3Er_2Cl_9$ derived from Fig. 3 with the corresponding calculated rates from Table III, both relative to the respective values for $^4S_{3/2}$. The calculated rates are those within the first 2% of the crystal length (first longitudinal element of the spatial resolution; cf. Appendix B). Weighting of the calculated rates from all five longitudinal elements $n=1-5$ leads to similar results, because in $Cs_3Er_2Cl_9$ luminescence from the first element is dominant whereas in $Cs_3Lu_2Cl_9$:1% the pump absorption is weak and, therefore, relatively homogeneous in longitudinal direction.

Initial multiplet	Wavelength	$Cs_2Lu_2Cl_9$:1% Er^{3+} Expt.	$Cs_2Lu_2Cl_9$:1% Er^{3+} Calc.	$Cs_2Er_2Cl_9$ Expt.	$Cs_2Er_2Cl_9$ Calc.
$^4I_{9/2}$	~820 nm	2.71	1.9	2.01	0.18
$^4F_{9/2}$	~650 nm	0.02	8×10^{-5}	1.89	1.15
$^4S_{3/2}$	~550 nm	1.00	1.00	1.00	1.00
$^2H_{9/2}$	~420 nm	9×10^{-3}	2×10^{-5}	0.06	3×10^{-3}

Altogether, the solutions of the rate equations provide results which reproduce the measured behavior of upconversion luminescence in the chloride system with good agreement. We are, therefore, confident that our model, despite its approximate nature, accounts for the dominant excitation and relaxation processes in our system.

In addition to the direct comparison of the experimental and calculated results in $Cs_3Lu_2Cl_9$:1% Er^{3+} and $Cs_3Er_2Cl_9$, we can compare the derived ETU parameters of Table VI of Appendix A with ETU parameters reported for other host materials. Recently, reliable data of upconversion from $^4I_{13/2}$ (ETU_1 of Table VI of Appendix A) and $^4I_{11/2}$ (ETU_{11} of Table VI of Appendix A) have been reported for $LiYF_4$ and YSGG as a function of Er^{3+} concentration.[51] The dopant concentration of $N_d=45.25\times10^{20}\,cm^{-3}$ corresponds to 100% Er^{3+} in $Cs_3Lu_2Cl_9$, 33% Er^{3+} in $LiYF_4$, and 36% Er^{3+} in YSGG, and we compare the upconversion parameters for these concentrations. The parameter for upconversion from $^4I_{13/2}$ (ETU_1) in our system, $W_{UC}=0.5\times10^{-22}\,m^3\,s^{-1}$ (Table VI of Appendix A), is smaller than the values of 1.3

TABLE V. Calculated steady-state population densities $N\,(\mathrm{m}^{-3})$ of the multiplets along the main excitation sequence $^4I_{15/2}\rightarrow{}^4I_{13/2}\rightarrow{}^4I_{9/2}\rightarrow{}^4S_{3/2}\rightarrow{}^2H_{9/2}$ at 1% and 100% dopant concentration for the highest available pump power of 20 mW cw within the first 2% of the crystal length (first longitudinal element of the spatial resolution; cf. Appendix B).

Multiplet	N (1%)	N (100%)
Dopant conc.	4.5×10^{25}	4.5×10^{27}
$^4I_{15/2}$	4.2×10^{25}	4.5×10^{27}
$^4I_{13/2}$	3.6×10^{24}	5.6×10^{25}
$^4I_{9/2}$	4.0×10^{21}	7.5×10^{24}
$^4S_{3/2}/{}^2H_{11/2}$	9.7×10^{19}	1.9×10^{24}
$^2H_{9/2}$	9.9×10^{15}	2.5×10^{22}

$\times10^{-22}\,\mathrm{m}^3\,\mathrm{s}^{-1}$ in $LiYF_4:Er^{3+}$ and $2.3\times10^{-22}\,\mathrm{m}^3\,\mathrm{s}^{-1}$ in YSGG:Er^{3+}.[51] For upconversion from $^4I_{11/2}$ (ETU_{11}), we obtain a value of $W_{UC}=1.2\times10^{-22}\,\mathrm{m}^3\,\mathrm{s}^{-1}$ (Table VI of Appendix A) which is also smaller than the values of $2.1\times10^{-22}\,\mathrm{m}^3\,\mathrm{s}^{-1}$ in $LiYF_4$ and $1.4\times10^{-22}\,\mathrm{m}^3\,\mathrm{s}^{-1}$ in YSGG.[51] For both ETU processes, however, the parameter range is within one order of magnitude when comparing the different host materials.

VI. EXCITATION AND RELAXATION MECHANISMS

In this section, we present a detailed analysis of the interplay of the relevant excitation and decay processes, investigate the population densities of the involved multiplets, and explain the relative rates (Fig. 3), the power dependence (Fig. 4), and the transient behavior (Fig. 5) of upconversion luminescence in the chloride system.

A. Mechanisms for cw excitation

The first excitation step is a GSA at 1.54 μm and leads to excitation of the $^4I_{13/2}$ level. This state is long lived and acts as an excitation reservoir (cf. the population densities of Table V) for subsequent upconversion steps which may take place by either ESA or ETU.

Under the pump conditions of our experiment, the steady-state population densities of the different excited states differ by orders of magnitude. Along the sequence $^4I_{13/2}\rightarrow{}^4I_{9/2}\rightarrow{}^4S_{3/2}\rightarrow{}^2H_{9/2}$ the population density within the first 2% of the crystal length (first longitudinal element of the spatial resolution of the calculation; cf. Appendix B) decreases by approximately one order of magnitude with each excitation step in the 100% sample (Table V). In the 1% sample, the decrease is approximately two to three orders of magnitude in each step, which is due to the decrease in the ETU transfer parameters W_t by three orders of magnitude from the 100% to the 1% sample (Appendix A).

The ESA transition $^4I_{9/2}\rightarrow{}^2H_{11/2}$ (Fig. 6) may be relevant for the excitation mechanisms because of its spectral overlap with GSA (Appendix B). Comparison of the rates of ESA and its competing upconversion process ETU_2 $(^4I_{13/2},{}^4I_{9/2})\rightarrow(^4I_{15/2},{}^2H_{11/2})$ in Table III shows that ESA is an important process in the 1% sample but negligible in the 100% sample. The reason is the strong dependence of the ETU transfer parameters W_t on dopant concentration (Appendix A) and, consequently, the increasing influence of ETU_2 in the 100% sample.

The ETU processes which are found to be most important for the excitation mechanisms are displayed in Fig. 6. For each process which has two possible pathways only the stronger pathway is shown. The arrows indicate the direction of upconversion, the reverse process is a cross relaxation. Whether an ETU rate is stronger in upconversion or cross-relaxation direction depends on the interplay of all relevant excitation and decay processes and may change with dopant concentration and pump power.

The distribution of the population density among the different excited levels, in combination with the lack of significant ground-state bleaching (Table V), clearly favors cross-relaxation processes which involve the ground state as well as ETU processes which involve the $^4I_{13/2}$ reservoir as one of their two initial states. The calculated ETU rates and the knowledge of the individual rates of upconversion and cross relaxation for each process (Table III) show that the four most relevant ETU processes are ETU_1, ETU_2, ETU_3, and ETU_4. These four processes are—in one direction—cross-relaxation processes which involve the $^4I_{15/2}$ ground state, and three of these four processes are—in the other direction—upconversion processes that involve $^4I_{13/2}$ as an initial state. They involve only states along the sequence $^4I_{15/2}\rightarrow{}^4I_{13/2}\rightarrow{}^4I_{9/2}\rightarrow{}^4S_{3/2}\rightarrow{}^2H_{9/2}$, which demonstrates the efficiency of this excitation sequence under 1.54-μm pumping in a chloride.

The processes ETU_1-ETU_4 compete with each other in populating and depleting the $^4I_{13/2}$, $^4I_{9/2}$, $^4S_{3/2}$, and $^2H_{9/2}$ levels. In the 1% sample, the population densities of these levels decrease by several orders of magnitude with each excitation step up to $^2H_{9/2}$ (Table V), leading to higher rates in the direction of upconversion for all four processes ETU_1-ETU_4. This can be seen in Table III: the effective ETU rates calculated from Eq. (A7) of Appendix A are almost equal to their upconversion rates, because these are much higher than the corresponding cross-relaxation rates. In the 100% sample, on the other hand, the much higher excited-state population densities up to $^2H_{9/2}$ result in high rates for the processes ETU_1-ETU_4 also in the direction of cross relaxation. This leads to effective ETU rates which are small compared to the corresponding rates in upconversion direction or are even negative if the cross-relaxation rate is higher than the upconversion rate (ETU_4 in Table III).

B. Upconversion luminescence rates

The relative ground-state luminescence rates from $^4I_{9/2}$ and $^4S_{3/2}$ around 820 and 550 nm, respectively, are comparable for both dopant concentrations (Fig. 3 and Table IV), despite the fact that excitation of $^4S_{3/2}$ requires three absorption steps compared to a two-step absorption for $^4I_{9/2}$. For 1% dopant concentration, ESA $^4I_{9/2}\rightarrow{}^2H_{11/2}$ is an important process, whereas in the 100% sample the process ETU_2 $(^4I_{13/2},{}^4I_{9/2})\rightarrow(^4I_{15/2},{}^2H_{11/2})$ is strong, see the large parameters σ_{ESA} (Appendix B) and W_{UC} (Table VI of Appendix A), respectively. Both processes deplete $^4I_{9/2}$ and populate $^4S_{3/2}/{}^2H_{11/2}$ which leads to a relatively high population density for the latter state. In addition, radiative decay from

$^4S_{3/2}$ has a large rate constant and is a significant decay mechanism for $^4S_{3/2}$, whereas the smaller radiative decay constant from $^4I_{9/2}$ leads to a competition of radiative decay with ESA or ETU_2 (Tables I and III).

For both dopant concentrations, the ground-state luminescence rate around 420 nm from $^2H_{9/2}$ (Fig. 3 and Table IV) is small compared to the luminescence rate from $^4I_{9/2}$ and $^4S_{3/2}$. In the 1% sample, this is due to the upconversion processes ETU_3 $(^4S_{3/2}, ^4I_{13/2}) \rightarrow (^4I_{15/2}, ^2H_{9/2})$ and ETU_4 $(^4I_{9/2}, ^4I_{9/2}) \rightarrow (^4I_{15/2}, ^2H_{9/2})$ having small rates compared to ETU_1, ETU_2, and ESA (Table III). The reason is the rapidly decreasing population density along the sequence $^4I_{13/2} \rightarrow ^4I_{9/2} \rightarrow ^4S_{3/2} \rightarrow ^2H_{9/2}$.

In the 100% sample, the $^2H_{9/2}$ luminescence rate increases but is still significantly smaller than the $^4I_{9/2}$ and $^4S_{3/2}$ luminescence. In this case, the reason is neither a small upconversion parameter of ETU_3 (cf. the values of W_{UC} for $ETU_{1\text{-}3}$ in Table VI of Appendix A), nor is the decrease in population density along the sequence $^4I_{13/2} \rightarrow ^4I_{9/2} \rightarrow ^4S_{3/2} \rightarrow ^2H_{9/2}$ very pronounced in the 100% sample. It is the highly competitive process ETU_4 $(^4I_{9/2}, ^4I_{9/2}) \rightarrow (^4I_{15/2}, ^2H_{9/2})$ which is now stronger in the cross-relaxation direction and, thus, depletes $^2H_{9/2}$ and quenches luminescence from this state (compare the rates of ETU_3, ETU_4, and LUM_8 for the 100% sample in Table III).

The rates of the other four ETU processes of Fig. 6, ETU_5-ETU_8, are smaller (Table III). They are not relevant for the excitation along the sequence $^4I_{15/2} \rightarrow ^4I_{13/2} \rightarrow ^4I_{9/2} \rightarrow ^4S_{3/2} \rightarrow ^2H_{9/2}$ but they are of importance for the population of the other excited levels. Specifically, the processes ETU_5 $(^4I_{11/2}, ^4F_{9/2}) \rightarrow (^4I_{13/2}, ^2H_{11/2})$ and ETU_8 $(^4F_{9/2}, ^4I_{13/2}) \rightarrow (^4I_{15/2}, ^4F_{5/2})$ have higher rates in the cross-relaxation direction and lead to the population of $^4F_{9/2}$ for both concentrations. However, there is a striking difference in the rates of these processes of at least four orders of magnitude between the 1% and 100% samples (Table III). This explains the experimental finding that the ground-state luminescence around 650 nm from $^4F_{9/2}$ is practically absent in the 1% sample but increases significantly in the 100% sample [cf. Figs. 3(a) and 3(b)], an effect which is reproduced in the calculations (cf. the rates of LUM_4 in Table III).

C. Power dependence of upconversion luminescence

If an upper excited state is mainly populated by a dominant upconversion process from an intermediate state, the slope of the luminescence rate from the upper state versus pump power depends on the competition of linear decay rate with upconversion rate for the depletion of the intermediate state.[52] If the upconversion rates are negligible compared to the linear decay rates from the corresponding intermediate states for several successive upconversion steps, the order n of the excitation process, i.e., the number of photons n required for the excitation of the corresponding emitting level, can be extracted directly from the slope of the luminescence intensity versus pump power in double-logarithmic representation.[52]

The condition that upconversion rates are negligible compared to the linear decay rates of the intermediate states is approximately fulfilled for the 1% sample at low pump power. Even at the highest pump power of 20 mW (Table III), luminescence is still the dominating decay mechanism, although upconversion is not negligible anymore at higher pump power: $LUM_1 \gg ETU_1$; $LUM_3 > ESA$, ETU_2, ETU_4; $LUM_5 \gg ETU_3$.

The slopes of the luminescence intensities versus pump power in the 1% sample at low pump power, therefore, represent the number of excitation steps required for the population of the corresponding levels. The initial slopes measured in $Cs_3Lu_2Cl_9$:1% Er^{3+} [indicated in Fig. 4(a)] suggest a two-step upconversion process for the population of $^4I_{9/2}$, a three-step process for $^4S_{3/2}$, and a four-step process for $^2H_{9/2}$. This is expected for the excitation sequence $^4I_{15/2} \rightarrow ^4I_{13/2} \rightarrow ^4I_{9/2} \rightarrow ^4S_{3/2} \rightarrow ^2H_{9/2}$ and is clearly reproduced by the calculated power dependence.

The measured slope for $^4F_{9/2}$ in the 1% sample is slightly larger than for $^4S_{3/2}$ but smaller than for $^2H_{9/2}$. The calculation suggests a four-step excitation of $^4F_{9/2}$ along the sequence $^4I_{15/2} \rightarrow ^4I_{13/2} \rightarrow ^4I_{9/2} \rightarrow ^2H_{11/2} \rightarrow ^4F_{9/2}$, with the fourth step being a cross-relaxation process $(^2H_{11/2}, ^4I_{13/2}) \rightarrow (^4I_{11/2}, ^4F_{9/2})$ which requires the absorption of a fourth pump photon into $^4I_{13/2}$. Consequently, the calculated slope is close to 4 and similar to that of $^2H_{9/2}$ luminescence. The discrepancy between experiment and calculation may be due to additional excitation of $^4F_{9/2}$ by upconversion from lower-lying levels. A possible process is $(^4I_{13/2}, ^4I_{11/2}) \rightarrow (^4I_{15/2}, ^4F_{9/2})$ which is not included in our rate equations due to its large energy mismatch of four highest-energy phonons. A linear relaxation step $^2H_{11/2}/^4S_{3/2} \rightarrow ^4F_{9/2}$ is unlikely, because the radiative branching ratio $^2H_{11/2}/^4S_{3/2} \rightarrow ^4F_{9/2}$ is less than 0.1% (Table VII of Appendix B) and multiphonon relaxation is extremely inefficient in the chloride system with the large energy gap $^4S_{3/2}$-$^4F_{9/2}$.

A completely different situation obtains if nonlinear upconversion rates dominate over linear decay rates for the depletion of the intermediate states. The slope in the power dependence of luminescence from the highest-lying state is expected to converge to one, whereas the slopes of the intermediate excited states will even be smaller than one.[52] If the relevant upconversion processes are ETU rather than ESA processes and the linear decay occurs predominantly via ground-state luminescence, the slopes of luminescence from intermediate excited states are expected to converge to 0.5.[52]

These conditions are approximately fulfilled in $Cs_3Er_2Cl_9$ at high pump power (Table III): The main ETU processes $ETU_{1\text{–}4}$ have higher rates than the luminescent processes $LUM_{2\text{–}5}$, ETU_2 is stronger than ESA, and the dominant linear decay is ground-state luminescence (cf. the branching ratios in Table VII of Appendix B). Measured and calculated graphs for $Cs_3Er_2Cl_9$ [Fig. 4(b)] show that the slope for the $^2H_{9/2}$ luminescence intensity converges to one at higher pump power, whereas the slopes of the luminescence intensities from intermediate excited states become equal to each other at high pump power and slowly converge to a slope of 0.5, in excellent agreement between experiment and calculation.

The pronounced differences in the observed power dependences between $Cs_3Lu_2Cl_9$:1% Er^{3+} and $Cs_3Er_2Cl_9$ and the surprisingly small slopes in the latter can, thus, be quantitatively reproduced by our model. At low dopant concentration, the linear decay of the intermediate state is much faster than the nonlinear upconversion process which feeds the up-

per state. At high dopant concentration, the hierarchy is reversed, leading to much weaker power dependences.

D. Transient behavior

The $^4I_{9/2}$ and $^4S_{3/2}$ transients in $Cs_3Er_2Cl_9$ [Fig. 5(b)] are very similar. The luminescence intensities increase sharply during the pump-pulse duration of 100 μs, and after reaching a peak at 300 μs they decay almost exponentially. If a short-lived excited state is mainly populated by one dominant upconversion process from a longer-lived intermediate state, the rise time of the upconversion transient corresponds to the lifetime of the upper state and the decay part of the transient to the lifetime of the intermediate state.[53] This condition is nearly fulfilled for the processes ETU_1 $(^4I_{13/2}, {}^4I_{13/2}) \rightarrow (^4I_{15/2}, {}^4I_{9/2})$ and ETU_2 $(^4I_{13/2}, {}^4I_{9/2}) \rightarrow (^4I_{15/2}, {}^2H_{11/2})$ in $Cs_3Er_2Cl_9$; see Fig. 6. The short rise time of the $^4I_{9/2}$ and $^4S_{3/2}$ transients reflects the lifetime quenching of these states by cross relaxation at high dopant concentration and high temperature (Table I). The following 1/*e* decay times of the $^4I_{9/2}$ and $^4S_{3/2}$ transients of 7 and 5 ms, respectively, are only slightly smaller than the decay times of the corresponding feeding states $^4I_{13/2}$ (intrinsic lifetime 12.3 ms) and $^4I_{9/2}$ (the 1/*e* decay time of 7 ms mentioned above).

The $^4I_{9/2}$ transient in $Cs_3Lu_2Cl_9$:1% Er^{3+} [Fig. 5(a)] shows a slow rise and a peak after 8 ms which reflects the unquenched $^4I_{9/2}$ lifetime of 9.8 ms at low dopant concentration (Table I). This is followed by a decay with a 1/*e* decay time of 10 ms, again indicative of the process ETU_1 $(^4I_{13/2}, {}^4I_{13/2}) \rightarrow (^4I_{15/2}, {}^4I_{9/2})$ populating the $^4I_{9/2}$ multiplet from the $^4I_{13/2}$ reservoir.

The $^4S_{3/2}$ transient in $Cs_3Lu_2Cl_9$:1% Er^{3+} [Fig. 5(a)] exhibits a very different behavior. A sharp rise with a duration of the pump pulse of 100 μs and a subsequent fast decay with a 1/*e* decay time of 430 μs which is similar to the $^4S_{3/2}$ lifetime of 390 μs (Table I) reflect the ESA process $^4I_{9/2} \rightarrow {}^2H_{11/2}$ which populates $^4S_{3/2}/{}^2H_{11/2}$ during the pump pulse. This is followed by a slow decay with a decay time similar to that of the $^4I_{9/2}$ transient which shows the influence of ETU_2 $(^4I_{13/2}, {}^4I_{9/2}) \rightarrow (^4I_{15/2}, {}^2H_{11/2})$. The fact that the calculated curve shows a second peak which is absent in the measured curve is at least partly explained by the uncertainty in the ESA cross section and the transfer parameters W_t for the 1% sample which determine the relative rates of ESA and ETU_2 and, therefore, the relative height of the two peaks in the $^4S_{3/2}$ transient.

Concerning the relative influence of ESA and ETU_2, two aspects are important. On the one hand, the height of the peak during the pump pulse compared to that of the long-lived tail shows that the ESA rate is higher than the rate of ETU_2, in agreement with the results obtained for cw excitation (cf. the rates of ESA and ETU_2 in Table III). On the other hand, the time integrals of the two parts show that the contribution of ETU_2 to the overall $^4S_{3/2}/{}^2H_{11/2}$ population and the time-integrated $^4S_{3/2}$ luminescence is larger. This is a consequence of the time scales of 100 μs (pump-pulse duration) and 10 ms ($^4I_{13/2}$ and $^4I_{9/2}$ lifetimes) at which the contributions from ESA and ETU_2, respectively, occur.

The transients of Fig. 5 are normalized for peak height. The absolute peak intensities calculated from the rate equations are two and five orders of magnitude smaller for $^4S_{3/2}$ luminescence in the 100% and 1% samples, respectively, compared to the $^4I_{9/2}$ luminescence. The reason is that the short pump-pulse duration of 100 μs cannot efficiently populate the $^4I_{13/2}$ state with its long lifetime of 12.3 ms. Consequently, the steady-state population densities of Table V are not reached, and ETU as well as ESA are much less efficient than for cw excitation. This also explains increased noise in the measured $^4S_{3/2}$ luminescence curve.

VII. CONCLUSIONS

We have studied upconversion luminescence in $Cs_3Lu_2Cl_9$:1% Er^{3+}, $Cs_3Lu_2Br_9$:1% Er^{3+}, and $Cs_3Y_2I_9$:1% Er^{3+} as well as in the concentrated systems $Cs_3Er_2X_9$ (X = Cl, Br, I) for pulsed and cw laser excitation at 1.54 μm. By maintaining the crystal structure and varying the chemical environment of Er^{3+} along the halide series we can study the effect of this chemical coordinate on the physical behavior. Concentration is another very important variable in this study. It turns out that the $Cs_3Lu_2Cl_9$:1% Er^{3+} and $Cs_3Er_2Cl_9$ samples have distinctly different excited-state dynamics. It is an excellent test of the model that these experimental trends can be reproduced. The measurement of relative upconversion intensities under cw excitation, power dependences as well as excitation transients provides a broad experimental basis for a very comprehensive study of upconversion processes in this series of compounds.

The variation of the chemical structure showed that decreasing optical phonon frequencies for chloride, bromide, and iodide, as well as decreasing crystal-field strengths contribute significantly to the suppression of $^4I_{9/2}$ multiphonon relaxation, resulting in long $^4I_{9/2}$ lifetimes compared to oxides and fluorides. Efficient two-, three-, and four-step upconversion excitation is, therefore, possible along the sequence $^4I_{15/2} \rightarrow {}^4I_{13/2} \rightarrow {}^4I_{9/2} \rightarrow {}^4S_{3/2} \rightarrow {}^2H_{9/2}$, in distinct contrast to the behavior usually found for oxides and fluorides for these pump conditions.

The large set of data obtained from the spectroscopic measurements for both dopant concentrations in the chloride system has provided enough information for the calculation of the complex excitation and depletion mechanisms in a rate-equation model. Without any fit parameter for the calculation of the $Cs_3Er_2Cl_9$ data and only one fit parameter used for $Cs_3Lu_2Cl_9$:1% Er^{3+}, the results of the intensity, power-dependence, and transient measurements are reproduced by the calculation with good qualitative and quantitative agreement, thus enabling the identification of the processes which underly the measured behavior.

Time-resolved spectroscopy and numerical investigations show that, after GSA $^4I_{15/2} \rightarrow {}^4I_{13/2}$, the upconversion steps $^4I_{13/2} \rightarrow {}^4I_{9/2}$ and $^4S_{3/2} \rightarrow {}^2H_{9/2}$ occur by ETU. ESA and ETU are in competition for the $^4I_{9/2} \rightarrow {}^4S_{3/2}/{}^2H_{11/2}$ upconversion step because of the good spectral overlap of ESA and GSA of within 3 cm^{-1}. Whereas ETU is the dominant mechanism for this step at high dopant concentration, it becomes less efficient than ESA at low dopant concentration.

The four ETU processes $(^4I_{13/2}, {}^4I_{13/2}) \rightarrow (^4I_{15/2}, {}^4I_{9/2})$, $(^4I_{13/2}, {}^4I_{9/2}) \rightarrow (^4I_{15/2}, {}^2H_{11/2})$, $(^4S_{3/2}, {}^4I_{13/2}) \rightarrow (^4I_{15/2}, {}^2H_{9/2})$, and $(^4I_{9/2}, {}^4I_{9/2}) \rightarrow (^4I_{15/2}, {}^2H_{9/2})$ contribute to the main excitation steps along the sequence $^4I_{15/2} \rightarrow {}^4I_{13/2} \rightarrow {}^4I_{9/2} \rightarrow {}^4S_{3/2} \rightarrow {}^2H_{9/2}$. Whereas at low dopant concentration

these processes are stronger in the direction of upconversion and are followed by luminescent decay, they compete with each other for the population and depletion of the excited levels at high dopant concentration.

The change in the mechanisms from predominant linear decay to predominant depletion by upconversion and cross relaxation with increasing dopant concentration and pump power also explains the surprising power dependence of the measured upconversion-luminescence rates. Their slopes in double-logarithmic representation change completely from n for n-step excitation at low pump power in the 1% sample to a linear dependence for $^2H_{9/2}$ and a square-root dependence for the intermediate excited levels at strong excitation in the 100% sample. This result is expected from theory[52] and reproduced with excellent accuracy in the calculation.

ACKNOWLEDGMENTS

We are indebted to S. C. Rand, University of Michigan for supporting this collaboration and providing laboratory space and equipment. We thank T. R. Gosnell from Los Alamos National Laboratory for providing a calibration lamp. The 1.54-μm laser system was provided by CST-1, Los Alamos National Laboratory. It is a pleasure to acknowledge the assistance of K. Krämer and N. Furer with the crystal growth. The computer source code was developed during earlier works at the Institute of Applied Physics, University of Bern, Switzerland, and the Optoelectronics Research Centre, University of Southampton, United Kingdom. This work was financially supported by the Swiss National Science Foundation.

APPENDIX A: MODELING OF ENERGY-TRANSFER PROCESSES

In this appendix, we discuss the approach to calculating the probability of possible ETU processes and give the parameters and equations for the calculation of the rates of these processes. The model operates on the level of multiplets and thus neglects specific crystal-field splittings. The total crystal-field splitting of a given multiplet is taken as the width of this multiplet. All two-ion energy-transfer processes which exhibit either a direct overlap of energies or an energy mismatch of less than one maximum phonon energy ($E_{\mathrm{ph,max}}=260\,\mathrm{cm}^{-1}$ in the chloride) are considered in the calculation.

We define here $E_{\min}$ and $E_{\max}$ as the energies of the longest- and shortest-wavelength multiplet-to-multiplet transition, respectively, whose spectral lineshape, therefore, ranges from $E_{\min}$ to $E_{\max}$. A direct spectral overlap between a donor line shape ranging from $E_{D,\min}$ to $E_{D,\max}$ and an acceptor line shape ranging from $E_{A,\min}$ to $E_{A,\max}$ is present if the conditions

$$E_{D,\min}<E_{A,\max} \quad \text{and} \quad E_{A,\min}<E_{D,\max} \tag{A1}$$

are fulfilled. The process is exothermic, i.e., one phonon is emitted during the transition, if

$$0<E_{D,\min}-E_{A,\max}<E_{ph,\max}. \tag{A2}$$

On the other hand, the process is endothermic, i.e., one phonon is absorbed during the transition, if

$$0<E_{A,\min}-E_{D,\max}<E_{ph,\max} \tag{A3}$$

If an upconversion process is exothermic, its inverse process, i.e., the corresponding cross-relaxation process, is endothermic and vice versa.

With the known Stark-level energies of all relevant multiplets,[31] we find 35 upconversion processes which fulfill either Eq. (A1), (A2), or (A3) and which may play an important role in the excitation mechanisms in the chloride system (Table VI). Their inverse processes, i.e., the corresponding cross-relaxation processes, are also considered. In addition, those processes that do not start from the same initial level on both ions generally have two possible pathways with different transition probabilities in both upconversion and cross-relaxation direction, e.g., $(^4I_{13/2}, {}^4S_{3/2}) \rightarrow (^4I_{15/2}, {}^2H_{9/2})$ and $(^4I_{13/2}, {}^4S_{3/2}) \rightarrow (^2H_{9/2}, {}^4I_{15/2})$ are two pathways of the same upconversion process. These two pathways lead to the same result and cannot be distinguished by spectroscopic means. This accounts for 25 of the 35 energy-transfer processes of Table VI. In total, 35 ETU processes with $25\times2\times2+10\times2=120$ different pathways were included in the calculation.

Obviously it is impossible, even with a large amount of spectroscopic data, to determine the parameters of all these ETU processes. However, we can first compare these processes relative to each other by exploiting Dexter's equation for electric dipole-dipole energy transfer[54]

$$P_{\mathrm{DA}}\sim R^{-6}Q_DQ_A\int S_D(E)S_A(E)E^{-2}dE. \tag{A4}$$

The microscopic transition probability P_{DA} of the donor-acceptor transfer depends, first, on the product of the integral cross sections Q_D and Q_A of the involved donor and acceptor transitions, respectively, second, on the spectral overlap integral of the two line shapes $S_D(E)$ and $S_A(E)$, and, third, on the site structure of the host material which defines the donor-acceptor distance R.

The integral cross sections Q_D and Q_A are proportional to the oscillator strengths f_D and f_A of the donor and acceptor transitions, respectively. Oscillator strengths were obtained from a Judd-Ofelt calculation for $Cs_3Lu_2Cl_9$:1% Er^{3+} on the basis of the room-temperature multiplet-to-multiplet absorption intensities [Fig. 2(a)]. The Judd-Ofelt parameters from the least-squares fit were $\Omega_2=8.61$, $\Omega_4=0.423$, $\Omega_6=0.227$ (10^{-20} cm^2) using a refractive index of $n=1.82$.[33] In Table VI, F_{UC} and F_{CR} are the products of the oscillator strengths of donor and acceptor transitions for upconversion and cross relaxation, respectively. In the case of two possible pathways of an ETU process, products of both pathways for each process are summed for the F values. For an ETU process $(i,j)\rightarrow(k,l)$, this yields

$$F_{\mathrm{UC}}=f_{ik}f_{jl}+f_{il}f_{jk} \quad \text{and} \quad F_{\mathrm{CR}}=f_{ki}f_{lj}+f_{li}f_{kj}. \tag{A5}$$

If one of the initial levels is part of a combined level in the calculation ($^4S_{3/2}/{}^2H_{11/2}$ or $^4F_{5/2}/{}^4F_{3/2}$; see Appendix B), the F values are weighted by the Boltzmann factor of the corresponding initial level at 295 K (denoted by an asterisk in Table VI).

Concerning the spectral overlap integral, we consider the following experimental evidence. On the one hand, exother-

TABLE VI. ETU processes: donor and acceptor transition in upconversion direction. If two pathways are possible, the pathway with the higher oscillator strengths is given. Energy width ΔE (cm^{-1}) of direct spectral overlap ($\Delta E > 0\ cm^{-1}$) or energy mismatch ($-260\ cm^{-1} < \Delta E < 0\ cm^{-1}$, with ex indicating exothermic, en indicating endothermic) of donor and acceptor transition. F_{UC} and F_{CR} (10^{-12}) are calculated according to Eq. (A5). An asterisk denotes a F value that is weighted by the Boltzmann factor of the corresponding initial level at 295 K ($^4S_{3/2}$: 0.938; $^2H_{11/2}$: 0.062; $^4F_{5/2}$: 0.896; $^4F_{3/2}$: 0.104). According to Eq. (A6), W_{UC} and W_{CR} ($10^{-22}\ m^3\ s^{-1}$) are the products of the F values ($\times 10^{12}$) with the transfer parameters $W_{t,\mathrm{quasires}} = 3.6 \times 10^{-22}\ m^3\ s^{-1}$ or $W_{t,\mathrm{endoth}} = 0.28 \times 10^{-22}\ m^3\ s^{-1}$ for quasiresonant and endothermic processes, respectively. If an upconversion process is exothermic, the corresponding cross-relaxation process is endothermic and vice versa.

Process	Donor Trans	Acceptor Trans	ΔE	F_{UC}	F_{CR}	W_{UC}	W_{CR}
ETU_1	$^4I_{13/2} \rightarrow {}^4I_{15/2}$	$^4I_{13/2} \rightarrow {}^4I_{9/2}$	−204 ex	0.140	0.172	0.504	0.048
ETU_2	$^4I_{13/2} \rightarrow {}^4I_{15/2}$	$^4I_{9/2} \rightarrow {}^2H_{11/2}$	199	2.407	0.111*	8.665	0.400
ETU_3	$^4S_{3/2} \rightarrow {}^4I_{15/2}$	$^4I_{13/2} \rightarrow {}^2H_{9/2}$	44	0.479*	0.179	1.724	0.644
ETU_4	$^4I_{9/2} \rightarrow {}^4I_{15/2}$	$^4I_{9/2} \rightarrow {}^2H_{9/2}$	70	2.352	1.476	8.467	5.314
ETU_5	$^4I_{11/2} \rightarrow {}^4I_{13/2}$	$^4F_{9/2} \rightarrow {}^2H_{11/2}$	71	2.264	0.100*	8.150	0.360
ETU_6	$^4I_{11/2} \rightarrow {}^4I_{15/2}$	$^4I_{9/2} \rightarrow {}^4F_{5/2}$	−123 ex	0.146	0.165*	0.526	0.046
ETU_7	$^4I_{11/2} \rightarrow {}^4I_{15/2}$	$^4I_{9/2} \rightarrow {}^4F_{3/2}$	168	0.149	0.030*	0.536	0.108
ETU_8	$^4F_{9/2} \rightarrow {}^4I_{15/2}$	$^4I_{13/2} \rightarrow {}^4F_{5/2}$	−25 en	0.551	0.721*	0.154	2.596
ETU_9	$^4S_{3/2} \rightarrow {}^4I_{13/2}$	$^4I_{9/2} \rightarrow {}^2H_{9/2}$	−135 en	5.941*	1.810	1.663	6.516
ETU_{10}	$^2H_{11/2} \rightarrow {}^4I_{13/2}$	$^4I_{9/2} \rightarrow {}^2H_{9/2}$	−163 ex	0.624*	8.624	2.246	2.415
ETU_{11}	$^4I_{11/2} \rightarrow {}^4I_{15/2}$	$^4I_{11/2} \rightarrow {}^4F_{7/2}$	140	0.335	0.380	1.206	1.368
ETU_{12}	$^4I_{11/2} \rightarrow {}^4I_{13/2}$	$^4S_{3/2} \rightarrow {}^4F_{5/2}$	3	0.163*	0.089*	0.587	0.320
ETU_{13}	$^2H_{11/2} \rightarrow {}^4I_{13/2}$	$^4I_{11/2} \rightarrow {}^4F_{3/2}$	−23 ex	0.012*	0.052*	0.043	0.015
ETU_{14}	$^4I_{11/2} \rightarrow {}^4I_{13/2}$	$^4F_{7/2} \rightarrow {}^2H_{9/2}$	−194 en	1.028	0.705	0.288	2.538
ETU_{15}	$^4I_{9/2} \rightarrow {}^4I_{13/2}$	$^4I_{9/2} \rightarrow {}^4S_{3/2}$	166	0.018	0.031*	0.065	0.112
ETU_{16}	$^4S_{3/2} \rightarrow {}^4I_{11/2}$	$^4I_{9/2} \rightarrow {}^4F_{7/2}$	107	0.030*	0.013	0.108	0.047
ETU_{17}	$^4F_{7/2} \rightarrow {}^4I_{11/2}$	$^4I_{9/2} \rightarrow {}^4F_{3/2}$	−34 ex	0.196	0.034*	0.706	0.010
ETU_{18}	$^4F_{5/2} \rightarrow {}^4I_{11/2}$	$^4I_{9/2} \rightarrow {}^2H_{9/2}$	20	2.076*	1.158	7.474	4.169
ETU_{19}	$^4F_{3/2} \rightarrow {}^4I_{11/2}$	$^4I_{9/2} \rightarrow {}^2H_{9/2}$	−20 ex	1.310*	4.207	4.716	1.178
ETU_{20}	$^4F_{9/2} \rightarrow {}^4I_{9/2}$	$^4F_{9/2} \rightarrow {}^4S_{3/2}$	10	0.002	0.005*	0.007	0.018
ETU_{21}	$^4F_{9/2} \rightarrow {}^4I_{11/2}$	$^4F_{9/2} \rightarrow {}^4F_{7/2}$	98	0.330	0.343	1.188	1.235
ETU_{22}	$^2H_{11/2} \rightarrow {}^4I_{9/2}$	$^4F_{9/2} \rightarrow {}^4F_{5/2}$	64	0.026*	0.775*	0.094	2.790
ETU_{23}	$^4F_{5/2} \rightarrow {}^4I_{9/2}$	$^4F_{9/2} \rightarrow {}^2H_{9/2}$	−182 ex	1.004*	0.672	3.614	0.118
ETU_{24}	$^2H_{11/2} \rightarrow {}^4I_{11/2}$	$^4F_{9/2} \rightarrow {}^2H_{9/2}$	−122 en	0.415*	6.699	0.116	2.412
ETU_{25}	$^2H_{11/2} \rightarrow {}^4F_{9/2}$	$^4S_{3/2} \rightarrow {}^4F_{5/2}$	106	0.017*	0.212*	0.061	0.763
ETU_{26}	$^2H_{11/2} \rightarrow {}^4F_{9/2}$	$^4S_{3/2} \rightarrow {}^4F_{3/2}$	−111 en	0.045*	0.096*	0.013	0.346
ETU_{27}	$^4S_{3/2} \rightarrow {}^4I_{9/2}$	$^2H_{11/2} \rightarrow {}^2H_{9/2}$	−254 ex	0.005*	0.036	0.018	0.010
ETU_{28}	$^4S_{3/2} \rightarrow {}^4I_{9/2}$	$^4S_{3/2} \rightarrow {}^2H_{9/2}$	−209 en	0.002*	0.000	0.001	0.000
ETU_{29}	$^2H_{11/2} \rightarrow {}^4F_{9/2}$	$^4F_{7/2} \rightarrow {}^2H_{9/2}$	63	0.082*	1.272	0.295	4.579
ETU_{30}	$^4F_{7/2} \rightarrow {}^4S_{3/2}$	$^4F_{7/2} \rightarrow {}^4F_{3/2}$	2	0.000	0.000*	0.000	0.000
ETU_{31}	$^4F_{5/2} \rightarrow {}^4S_{3/2}$	$^4F_{7/2} \rightarrow {}^2H_{9/2}$	−91 en	0.079*	0.099*	0.022	0.356
ETU_{32}	$^4F_{3/2} \rightarrow {}^4S_{3/2}$	$^4F_{7/2} \rightarrow {}^2H_{9/2}$	16	0.036*	0.258*	0.130	0.929
ETU_{33}	$^4F_{7/2} \rightarrow {}^2H_{11/2}$	$^4F_{7/2} \rightarrow {}^4F_{5/2}$	−85 en	0.134	0.007*	0.038	0.025
ETU_{34}	$^4F_{5/2} \rightarrow {}^4F_{7/2}$	$^4F_{3/2} \rightarrow {}^2H_{9/2}$	−232 ex	0.000*	0.002	0.000	0.001
ETU_{35}	$^4F_{3/2} \rightarrow {}^4F_{7/2}$	$^4F_{3/2} \rightarrow {}^2H_{9/2}$	101	0.000*	0.000	0.000	0.000

mic processes according to Eq. (A2) can—by assistance of one phonon—reach a probability that is comparable to the strength of processes with direct spectral overlap according to Eq. (A1). A prominent example is the comparison of upconversion from $^4I_{13/2}$ (ETU_1 in Table VI) and $^4I_{11/2}$ (ETU_{11} in Table VI). The former is an exothermic process whereas the latter exhibits a direct spectral overlap of donor and acceptor line shapes. In $LiYF_4$ at a dopant concentration of $13.8 \times 10^{20}\ cm^{-3}$ (corresponding to 30% Er^{3+} concentration in $Cs_3Lu_2Cl_9$), the exothermic process has a parameter which is twice as large as the parameter of the process with direct spectral overlap.[51] This suggests that phonons also assist in bridging an energy mismatch between emission and absorption crystal-field transitions in the case of direct multiplet-multiplet spectral overlap according to Eq. (A1). This effect smoothens the spectral overlap integral, and we assume it to be the same for all investigated ETU processes which are either exothermic according to Eq. (A2) or exhibit a direct spectral overlap according to Eq. (A1). We will refer to these processes as ''quasiresonant'' processes in the following.

Therefore, we neglect the actual overlap between donor and acceptor line shapes and set the spectral overlap integral

in Eq. (A4) equal to unity for all ETU processes. In this approximation, the actual ETU parameters of each ETU process for upconversion W_{UC} and cross relaxation W_{CR} can be expressed by the products of the corresponding F values $[\times 10^{12}]$ of Table VI with a macroscopic transfer parameter W_t, respectively,

$$W_{UC} = W_t F_{UC}, \quad \text{and} \quad W_{CR} = W_t F_{CR}. \tag{A6}$$

On the other hand, many spectroscopic investigations have led to the conclusion that endothermic processes according to Eq. (A3) are less probable and have a smaller ETU parameter than quasiresonant processes. One prominent example is the comparison of upconversion from $^4I_{13/2}$ (ETU_1 in Table VI), which is an exothermic process, with its inverse process, cross relaxation from $^4I_{9/2}$, which is an endothermic process. In $LiYF_4$ at an Er^{3+} concentration of 33% which is equal to the Er^{3+} concentration in $Cs_3Er_2Cl_9$, the exothermic process has a parameter which is 12 times larger than the parameter of the endothermic process.[51] Therefore, we distinguish two cases for the transfer parameter W_t, one for quasiresonant ETU processes, $W_{t,\text{quasires}}$, and one for endothermic ETU processes, $W_{t,\text{endoth}}$. The above approximation for the spectral overlap integral is also made for endothermic processes according to Eq. (A3).

Thus, we have to determine two transfer parameters for ETU processes, $W_{t,\text{quasires}}$ and $W_{t,\text{endoth}}$. These can be derived for the 100% sample by reproducing the measured lifetime quenching of the $^4S_{3/2}/^2H_{11/2}$ and $^4I_{9/2}$ levels at 100% dopant concentration (Table I) owing to the cross-relaxation processes $(^2H_{11/2}, {}^4I_{15/2}) \rightarrow (^4I_{13/2}, {}^4I_{9/2})$ (ETU_2 in Table VI) and $(^4I_{9/2}, {}^4I_{15/2}) \rightarrow (^4I_{13/2}, {}^4I_{13/2})$ (ETU_1 in Table VI), respectively. The former is a quasiresonant process, whereas the latter is an endothermic process. The transfer parameters obtained in this way from Eqs. (A6),(A7), and the rate equations of Appendix B are $W_{t,\text{quasires}} = 3.6 \times 10^{-22}\ \text{m}^3\,\text{s}^{-1}$ and $W_{t,\text{endoth}} = 0.28 \times 10^{-22}\ \text{m}^3\,\text{s}^{-1}$ for 100% dopant concentration. The transfer parameter for quasiresonant processes is 13 times larger than that for endothermic processes, in good agreement with the above factor of 12 for $LiYF_4$.[51] This clearly supports our initial assumption that endothermic processes are less probable than quasiresonant processes and have to be treated separately.

We do not explicitly include energy migration in our rate equations but express its influence by the concentration dependence of the transfer parameters. Thus, for the 1% sample, we also have to find two transfer parameters. According to recent results for upconversion from $^4I_{11/2}$ (ETU_{11} in Table VI) in $LiYF_4:Er^{3+}$,[51] we assume a cubic dependence of the W_t parameters on dopant concentration, i.e., $W_{t,1\%} = 10^{-3} \times W_{t,100\%}$ for both $W_{t,\text{quasires}}$ and $W_{t,\text{endoth}}$. For upconversion from $^4I_{13/2}$ (ETU_1), a less pronounced concentration dependence has been found in Ref. 51. However, with the assumption of a quadratic concentration dependence agreement of calculated with experimental results could not be obtained for the 1% sample.

The transfer parameter W_t of Eq. (A6) also includes the transition from the microscopic description of Eq. (A4) to the macroscopic description of the rate equations of Appendix B, i.e., it contains information on the distribution of donor-acceptor distances R in the crystal. Since we calculate the transfer parameters $W_{t,\text{quasires}}$ and $W_{t,\text{endoth}}$ using the macroscopic rate equations of Appendix B, we do not have to apply a model which derives R either in a statistic way or by explicitly making use of the $Cs_3Lu_2Cl_9$ structure and averaging over all neighboring rare-earth sites.

The rate U of a given ETU process involving the transitions $(i,j) \rightarrow (k,l)$ is calculated as the difference of the rates of upconversion and corresponding cross-relaxation process,

$$U(\mathbf{r}) = W_{UC} N_i(\mathbf{r}) N_j(\mathbf{r}) - W_{CR} N_k(\mathbf{r}) N_l(\mathbf{r}), \tag{A7}$$

with W_{UC} and W_{CR} from Eq. (A6). If the initial states are different, i.e., $i \neq j$, the second pathway is implicitly considered in the F products of Eq. (A5). If the initial states are the same for both ions, i.e., $i = j$, the depletion rate for this state is $2 \times U$, which will be considered explicitly in the rate equations of Appendix B. A positive sign of U indicates that upconversion dominates over cross relaxation, whereas a negative sign indicates that the ETU process is stronger in the cross-relaxation direction.

The F and W_t values of all 35 ETU processes for 100% dopant concentration for both upconversion and cross-relaxation direction are summarized in Table VI. These values and the W_{UC} and W_{CR} values derived from Eq. (A6) are a useful approximation only at room temperature and above, for the following three reasons: First, the Judd-Ofelt analysis which provided the data for the calculation of the F products assumes infinite temperature. Second, the qualitative evaluation of the spectral overlap integral according to Eqs. (A1)–(A3) assumes comparable intensity of all crystal-field transitions which is possible only at high temperature. Third, endothermic processes according to Eq. (A3) require the absorption of one phonon. The corresponding phonon states are only populated at higher temperatures.

The W_{UC} and W_{CR} values of Table VI differ by more than three orders of magnitude among the investigated ETU processes. In addition, the population densities N of the initial states in Eq. (A7) differ by several orders of magnitude. This eliminates a number of ETU processes as relevant processes. The processes which are found to be most important for the excitation mechanisms under 1.54-μm pumping are displayed in Fig. 6. The rate equations which will be presented in Appendix B include only the important ETU processes of Fig. 6, although the source code considered all 35 ETU processes of Table VI in the calculation.

APPENDIX B: PARAMETERS AND RATE EQUATIONS

The computer simulation which was performed for the $Cs_3Lu_2Cl_9:Er^{3+}$ system involved all Er^{3+} levels up to $^2H_{9/2}$ (for the labeling, see Fig. 6) and the following processes and parameters: pump power and configuration, GSA and ground-state bleaching, ESA, all lifetimes and branching ratios, a large number of ETU processes, and the crystal data. In this appendix, we present all parameters used in the calculation and the rate equations implemented in the source code. For the modeling of the ETU processes, see Appendix A.

The $^4S_{3/2}$ and $^2H_{11/2}$ multiplets as well as the $^4F_{5/2}$ and $^4F_{3/2}$ multiplets are treated as combined levels in thermal equilibrium. The $Cs_3Lu_2Cl_9:Er^{3+}$ lifetimes τ_i of Fig. 6 represent the intrinsic lifetimes of the system at low dopant

TABLE VII. Radiative branching ratios β_{ij} for all excited states i to lower-lying states j as calculated from the Judd-Ofelt model using the parameters $\Omega_2=8.61$, $\Omega_4=0.423$, $\Omega_6=0.227$ (10^{-20} cm^2), and a refractive index of $n=1.82$ (Ref. 33). The radiative rate constants for $^2H_{11/2}/^4S_{3/2}$ and $^4F_{3/2}/^4F_{5/2}$ are weighted with their Boltzmann factors at 295 K of 0.062/0.938 and 0.104/0.896, respectively, and are summed for each transition in order to derive branching ratios for the combined levels.

Multiplet	$^4I_{15/2}$	$^4I_{13/2}$	$^4I_{11/2}$	$^4I_{9/2}$	$^4F_{9/2}$	$^2H_{11/2}/^4S_{3/2}$	$^4F_{7/2}$	$^4F_{3/2}/^4F_{5/2}$
$^2H_{9/2}$	0.051	0.163	0.070	0.646	0.064	0.003	0.003	0.000
$^4F_{3/2}/^4F_{5/2}$	0.397	0.377	0.078	0.098	0.040	0.007	0.003	
$^4F_{7/2}$	0.687	0.154	0.073	0.066	0.019	0.001		
$^2H_{11/2}/^4S_{3/2}$	0.671	0.268	0.020	0.041	0.000			
$^4F_{9/2}$	0.802	0.076	0.098	0.024				
$^4I_{9/2}$	0.776	0.196	0.028					
$^4I_{11/2}$	0.838	0.162						
$^4I_{13/2}$	1.000							

concentration and include only radiative decay. Multiphonon relaxations are neglected, because the maximum phonon energy is only 260 cm^{-1} in the chloride. The lifetimes of the $^4I_{13/2}$, $^4I_{9/2}$, and $^4S_{3/2}$ excited states are the values measured for $Cs_3Lu_2Cl_9$:1% Er^{3+} (Table I). The measured lifetime quenching of $^4I_{9/2}$ and $^4S_{3/2}$ in $Cs_3Er_2Cl_9$ at 295 K (Table I) is considered correctly in our rate equations by the corresponding cross-relaxation processes (cf. the detailed discussion in Appendix A). The lifetimes of the other excited states are the inverse of the sum of the radiative-decay rate constants obtained from the Judd-Ofelt calculation. Likewise, the branching ratios β_{ij} for the luminescent relaxations from an excited state i to lower-lying states j (Table VII) are taken from the Judd-Ofelt calculation which is based on the room-temperature multiplet-to-multiplet absorption intensities of $Cs_3Lu_2Cl_9$:1% Er^{3+} [Fig. 2(a)].

The crystal length is $l=2$ mm. The dopant concentrations are $N_d=0.4525\times10^{20}$ cm^{-3} (=1%) and $N_d=45.25\times10^{20}$ cm^{-3} (=100%). The pump-beam radius is $w_p=80\,\mu$m and the pump power is $P_{in}=20$ mW at the pump wavelength of $\lambda_p=1.536\,\mu$m. A fraction $\eta_{\rm in}=0.95$ of the pump power is launched into the sample. We define the atomic cross section σ_{ij} of a specific crystal-field transition from multiplet i to multiplet j as its effective absorption cross section $\sigma_{\rm eff}$ divided by the Boltzmann factor b_i of its initial Stark level, i.e., $\sigma_{ij}=\sigma_{\rm eff}/b_i$. The GSA atomic cross section at the pump wavelength of the $^4I_{15/2}(0)\rightarrow{}^4I_{13/2}(0)$ crystal-field transition, $\sigma_{01}=4.6\times10^{-20}$ cm^2, is derived from the measured effective absorption cross section at 295 K.

ESA on the transition $^4I_{9/2}\rightarrow{}^4S_{3/2}/^2H_{11/2}$ is possible from the $^4I_{9/2}(3)$ and $^4I_{9/2}(4)$ crystal-field levels at 12 509 and 12 513 cm^{-1} which are 129 and 133 cm^{-1} above $^4I_{9/2}(0)$, respectively. Transitions from these levels to the lowest $^2H_{11/2}(0)$ level have small energy mismatches of 3 and 1 cm^{-1} with the GSA transition, respectively.[31] At 295 K, these two levels have a combined thermal population of 29%, and $^4I_{9/2}\rightarrow{}^2H_{11/2}$ ESA is likely at this temperature. It was, therefore, included in the rate equations.

A Judd-Ofelt calculation predicts the cross section of $^4I_{9/2}\rightarrow{}^4S_{3/2}/^2H_{11/2}$ ESA to be twice that of the GSA transition. Since two ESA crystal-field transitions are excited at the pump wavelength, the ESA atomic cross section could be expected to be about 4 times the GSA cross section. However, this estimate is not necessarily accurate, because the cross sections obtained from Judd-Ofelt calculations represent multiplet-to-multiplet transitions only. Therefore, we treat the ESA cross section as the only free parameter in our model. ESA is of significant importance only in the 1% sample (cf. Sec. V). When comparing the measured and calculated transients of $^4S_{3/2}$ luminescence for the 1% sample [Fig. 5(a)], where ESA has a characteristic influence, reasonable agreement is obtained for an ESA atomic cross section of $\sigma_{35}=5.5\times10^{-19}$ cm^2 which is three times larger than expected from our rough estimate.

Since the pump power is almost entirely absorbed in the 100% sample, leading to a significant variation in population density over crystal length, and since the excitation mechanisms are highly nonlinear because of efficient ETU processes at higher dopant concentration, the calculation for the 100% sample had to be performed with spatial resolution. Let z and r be the variables of the longitudinal and radial coordinate within the crystal, respectively. They represent the discrete longitudinal elements $z=1$ to n covering the crystal length l as well as the discrete radial cylinder elements $r=1$ to m covering 1.5 times the waist radius w_p of the Gaussian pump beam. The elements are chosen with a progression in length from front surface to back surface of the crystal (2, 3, 4, 7, and 84%), thus providing a finer resolution at the front region where the contribution of the investigated processes is more significant.

A finite-element resolution of $n=m=5$ was chosen for the calculation. A higher longitudinal resolution does not significantly alter the calculated results for the 100% sample. The longitudinal resolution does not influence the calculation for the 1% sample, because the pump absorption is weak and, therefore, relatively homogeneous in longitudinal direction. Despite the nonlinearities involved, the radial resolution and assumption of a Gaussian pump beam with waist radius w_p leads to results which are very similar to those obtained when assuming a homogeneously pumped cylinder of radius w_p, in agreement with earlier findings.[55]

With $\mathbf{r}=(r,z)$, the space vector, $r_1(r)$ and $r_2(r)$, the inner and outer radii of the radial element r, respectively, and $\Delta l(z)$, the length of the longitudinal element z, the rate equations for the population densities $N_i(\mathbf{r})$ of the states indicated in Fig. 6 read

$$dN_8(\mathbf{r})/dt=-\tau_8^{-1}N_8(\mathbf{r})+U_3(\mathbf{r})+U_4(\mathbf{r}), \qquad \text{(B1)}$$

$$dN_7(\mathbf{r})/dt=\beta_{87}\tau_8^{-1}N_8(\mathbf{r})-\tau_7^{-1}N_7(\mathbf{r})+U_6(\mathbf{r})+U_7(\mathbf{r})+U_8(\mathbf{r}), \tag{B2}$$

$$dN_6(\mathbf{r})/dt=\Sigma_{i=7\cdots8}[\beta_{i6}\tau_i^{-1}N_i(\mathbf{r})]-\tau_6^{-1}N_6(\mathbf{r}), \tag{B3}$$

$$dN_5(\mathbf{r})/dt=R_{35}(\mathbf{r})+\Sigma_{i=6\cdots8}[\beta_{i5}\tau_i^{-1}N_i(\mathbf{r})]-\tau_5^{-1}N_5(\mathbf{r})+U_2(\mathbf{r})-U_3(\mathbf{r})+U_5(\mathbf{r}), \tag{B4}$$

$$dN_4(\mathbf{r})/dt=\Sigma_{i=5\cdots8}[\beta_{i4}\tau_i^{-1}N_i(\mathbf{r})]-\tau_4^{-1}N_4(\mathbf{r})-U_5(\mathbf{r})-U_8(\mathbf{r}), \tag{B5}$$

$$dN_3(\mathbf{r})/dt=-R_{35}(\mathbf{r})+\Sigma_{i=4\cdots8}[\beta_{i3}\tau_i^{-1}N_i(\mathbf{r})]-\tau_3^{-1}N_3(\mathbf{r})+U_1(\mathbf{r})-U_2(\mathbf{r})-2U_4(\mathbf{r})-U_6(\mathbf{r})-U_7(\mathbf{r}), \tag{B6}$$

$$dN_2(\mathbf{r})/dt=\Sigma_{i=3\cdots8}[\beta_{i2}\tau_i^{-1}N_i(\mathbf{r})]-\tau_2^{-1}N_2(\mathbf{r})-U_5(\mathbf{r})-U_6(\mathbf{r})-U_7(\mathbf{r}), \tag{B7}$$

$$dN_1(\mathbf{r})/dt=R_{01}(\mathbf{r})+\Sigma_{i=2\cdots8}[\beta_{i1}\tau_i^{-1}N_i(\mathbf{r})]-\tau_1^{-1}N_1(\mathbf{r})-2U_1(\mathbf{r})-U_2(\mathbf{r})-U_3(\mathbf{r})+U_5(\mathbf{r})-U_8(\mathbf{r}), \tag{B8}$$

$$N_d=\Sigma_{i=0\cdots8}N_i(\mathbf{r}). \tag{B9}$$

The ETU rates U_i are calculated from Eq. (A7) of Appendix A. For clarity, only the important ETU processes shown in Fig. 6 are considered in the rate equations (B1)–(B9), although the calculation included all 35 ETU processes of Table VI of Appendix A. The calculation of GSA and ESA pump rates considers stimulated emission at the pump wavelength. The absorption coefficient is

$$\alpha(\mathbf{r})=\sigma_{01}[b_0N_0(\mathbf{r})-b_1N_1(\mathbf{r})]+\sigma_{35}[b_3N_3(\mathbf{r})-b_5N_5(\mathbf{r})]. \tag{B10}$$

The Boltzmann factors of the initial and terminal Stark levels of GSA and ESA at 295 K are $b_0=0.228$ for $^4I_{15/2}(0)$, $b_1=0.214$ for $^4I_{13/2}(0)$, $b_3=0.148+0.145=0.293$ for $^4I_{9/2}(3+4)$, and $b_5=0.014$ for $^2H_{11/2}(0)$. The fraction $\rho_p(\mathbf{r})$ of the power of the Gaussian pump beam contained in the cylinder at $\mathbf{r}$ compared with the total pump power in the longitudinal element z is[56]

$$\rho_p(\mathbf{r})=2/[\pi w_p^2]\int_{r_1(r)}^{r_2(r)}\exp[-2r''^2/w_p^2]2\pi r''dr''=\exp[-2r_1^2(r)/w_p^2]-\exp[-2r_2^2(r)/w_p^2]. \tag{B11}$$

The power $P_l(z)$ which is launched into the longitudinal element z is calculated as[57]

$$P_l(z)=\eta_{\mathrm{in}}P_{\mathrm{n}}\prod_{z'=1}^{z-1}\left\{\sum_{r'=1}^{m}[\rho_p(\mathbf{r}')\exp(-\Delta l(z')\alpha(\mathbf{r}'))]\right\}. \tag{B12}$$

Equations (B11) and (B12) imply that after absorption of the pump power in each longitudinal element a Gaussian pump shape is maintained, i.e., a possible degradation of the Gaussian pump shape due to ground-state bleaching and, therefore, radially nonuniform absorption is neglected. Since the pump laser operated in the TEM_{00} mode and the samples were short, the divergence of the pump beam is also neglected in the calculation. With Eqs. (B10)–(B12), the equations for the pump rates $R_{01}(\mathbf{r})$ of GSA and $R_{35}(\mathbf{r})$ of ESA per unit volume read

$$R_{ij}(\mathbf{r})=\frac{\sigma_{ij}(b_iN_i-b_jN_j)}{\alpha(\mathbf{r})}\{1-\exp[-\Delta l(z)\alpha(\mathbf{r})]\}\times\frac{\lambda_p}{hc}\frac{P_l(z)\rho_p(\mathbf{r})}{\Delta l(z)\pi[r_2^2(r)-r_1^2(r)]}. \tag{B13}$$

h and c denote Planck's constant and the vacuum speed of light, respectively. The rate equations are solved in a Runge-Kutta calculation of fourth order.

*Present address: Department of Chemistry, The University Of Queensland, Brisbane QLD 4072, Australia.
†Present address: Gemfire Corporation, 2471 East Bayshore Road, Palo Alto, California 94303.

[1] F. E. Auzel, Proc. IEEE **61**, 758 (1973).
[2] J. C. Wright, in *Topics in Applied Physics: Radiationless Processes in Molecules and Condensed Phases*, edited by F. K. Fong (Springer, Berlin, 1976).
[3] *Modern Problems in Condensed Matter Sciences: Spectroscopy of Solids Containing Rare-Earth Ions*, edited by A. A. Kaplyanskii and R. M. Macfarlane (North-Holland, Amsterdam, 1987).
[4] L. F. Johnson, H. J. Guggenheim, T. C. Rich, and F. W. Ostermayer, J. Appl. Phys. **43**, 1125 (1972).
[5] Y. Mita, Appl. Phys. Lett. **39**, 587 (1981).
[6] S. A. Pollack, D. B. Chang, R. A. McFarlane, and H. Jenssen, J. Appl. Phys. **67**, 648 (1990).
[7] J. P. van der Ziel, L. G. Van Uitert, W. H. Grodkiewicz, and R. M. Mikulyak, J. Appl. Phys. **60**, 4262 (1986).
[8] S. A. Pollack and D. B. Chang, J. Appl. Phys. **64**, 2885 (1988).
[9] S. A. Pollack, D. B. Chang, and M. Birnbaum, Appl. Phys. Lett. **54**, 869 (1989).
[10] P. Xie and S. C. Rand, Appl. Phys. Lett. **60**, 3084 (1992).
[11] P. Xie and S. C. Rand, Opt. Lett. **17**, 1116 (1992).
[12] R. M. Macfarlane, E. A. Whittaker, and W. Lenth, Electron. Lett. **28**, 2136 (1992).
[13] P. Xie and S. C. Rand, Appl. Phys. Lett. **63**, 3125 (1993).
[14] S. A. Pollack, D. B. Chang, and N. L. Moise, J. Appl. Phys. **60**, 4077 (1986).
[15] S. A. Pollack, D. B. Chang, and N. L. Moise, Appl. Phys. Lett. **49**, 1578 (1986).
[16] P. Xie and S. C. Rand, Opt. Lett. **15**, 848 (1990).
[17] J. P. Jouart and G. Mary, J. Lumin. **46**, 39 (1990).
[18] E. Chiklis and L. Esterowitz, Phys. Rev. Lett. **21**, 1149 (1968).
[19] S. A. Pollack, D. B. Chang, I-Fu Shih, and R. Tzeng, Appl. Opt. **26**, 4400 (1987).
[20] G. S. Maciel, L. de S. Menezes, A. S. L. Gomes, C. B. de Araújo, Y. Messaddeq, A. Florez, and M. A. Aegerter, IEEE Photonics Technol. Lett. **7**, 1474 (1995).

[21] C. B. de Araújo, L. de S. Menezes, G. S. Maciel, L. H. Acioli, A. S. L. Gomes, Y. Messaddeq, A. Florez, and M. A. Aegerter, Appl. Phys. Lett. **68**, 602 (1996).
[22] G. S. Maciel, C. B. de Araújo, Y. Messaddeq, and M. A. Aegerter, Phys. Rev. B **55**, 6335 (1997).
[23] F. Auzel, J. Lumin. **31&32**, 759 (1984).
[24] F. Auzel, P. A. Santa-Cruz, and G. F. de Sá, Rev. Phys. Appl. **20**, 273 (1985).
[25] D. J. Simkin, J. A. Konigstein, P. Myslinski, S. A. Boothroyd, and J. Chrostowski, J. Appl. Phys. **73**, 8046 (1993).
[26] J. Thøgersen, N. Bjerre, and J. Mark, Opt. Lett. **18**, 197 (1993).
[27] T. Hebert, R. Wannemacher, W. Lenth, and R. M. Macfarlane, Appl. Phys. Lett. **57**, 1727 (1990).
[28] J. Ohwaki and Y. Wang, Jpn. J. Appl. Phys., Part 2 **31**, L1481 (1992).
[29] J. Ohwaki and Y. Wang, Electron. Lett. **29**, 351 (1993).
[30] J. Ohwaki and Y. Wang, Jpn. J. Appl. Phys., Part 2 **33**, L334 (1994).
[31] S. R. Lüthi, H. U. Güdel, M. P. Hehlen, and J. R. Quagliano, Phys. Rev. B **57**, 15 229 (1998).
[32] M. P. Hehlen, H. U. Güdel, and J. R. Quagliano, J. Chem. Phys. **101**, 10 303 (1994).
[33] S. R. Lüthi, H. U. Güdel, and M. P. Hehlen, J. Chem. Phys. (to be published).
[34] M. P. Hehlen, K. Krämer, H. U. Güdel, R. A. McFarlane, and R. N. Schwartz, Phys. Rev. B **49**, 12 475 (1994).
[35] M. P. Hehlen, G. Frei, and H. U. Güdel, Phys. Rev. B **50**, 16 264 (1994).
[36] G. Meyer, Z. Anorg. Allg. Chem. **455**, 140 (1978).
[37] G. Meyer, Prog. Solid State Chem. **14**, 141 (1982).
[38] F. A. Cotton and G. Wilkinson, *Advanced Inorganic Chemistry*, 4th ed. (Wiley, New York, 1980).
[39] G. Meyer, *Synthesis of Lanthanide and Actinide Compounds* (Kluwer, Dordrecht, 1991).
[40] S. H. Wang, S. M. Zuo, H. Eick, K. Krämer, and G. Meyer, J. Less-Common Met. **155**, 45 (1989).
[41] K. Krämer, Ph.D. thesis, University of Giessen, Germany, 1991.
[42] J. B. Gruber, J. R. Quagliano, M. F. Reid, F. S. Richardson, M. E. Hills, M. D. Seltzer, S. B. Stevens, C. A. Morrison, and T. H. Allik, Phys. Rev. B **48**, 15 561 (1993).
[43] W. T. Carnall, G. L. Goodman, R. S. Rana, P. Vandevelde, L. Fluyt, and C. Görller-Walrand, J. Less-Common Met. **116**, 17 (1986).
[44] R. A. McFarlane, J. Opt. Soc. Am. B **8**, 2009 (1991).
[45] R. A. McFarlane (private communication); the data are published in M. Pollnau, Ph.D. thesis, University of Hamburg, Germany, 1996.
[46] F. S. Richardson, M. F. Reid, J. J. Dallara, and R. D. Smith, J. Chem. Phys. **83**, 3813 (1985).
[47] K. W. Krämer, H. U. Güdel, and R. N. Schwartz, Phys. Rev. B **56**, 13 830 (1997).
[48] J. R. Quagliano, N. J. Cockroft, K. E. Gunde, and F. S. Richardson, J. Chem. Phys. **105**, 9812 (1996).
[49] J. M. F. van Dijk and M. F. H. Schuurmans, J. Chem. Phys. **78**, 5317 (1983).
[50] M. P. Hehlen, N. J. Cockroft, T. R. Gosnell, and A. J. Bruce, Phys. Rev. B **56**, 9302 (1997).
[51] T. Jensen, Ph.D. thesis, Institute of Laser-Physics, University of Hamburg, 1996.
[52] M. Pollnau, D. R. Gamelin, S. R. Lüthi, H. U. Güdel, and M. P. Hehlen (unpublished).
[53] J. Rubin, A. Brenier, R. Moncorgé, and C. Pedrini, J. Lumin. **36**, 39 (1986).
[54] D. L. Dexter, J. Chem. Phys. **21**, 836 (1953).
[55] M. Pollnau, P. J. Hardman, W. A. Clarkson, and D. C. Hanna, Opt. Commun. **147**, 203 (1998).
[56] W. P. Risk, J. Opt. Soc. Am. B **5**, 1412 (1988).
[57] M. Pollnau, IEEE J. Quantum Electron. **33**, 1982 (1997).